

# A Stable, Accurate and Well-Conditioned Time-Domain PMCHWT Formulation

Van Chien Le, *Member, IEEE*, Cedric Münger, *Member, IEEE*, Francesco P. Andriulli, *Fellow, IEEE*, and Kristof Cools, *Member, IEEE*

arXiv:2510.07989v1 [eess.SY] 9 Oct 2025

**Abstract**—This paper introduces a new boundary element formulation for transient electromagnetic scattering by homogeneous dielectric objects based on the time-domain PMCHWT equation. To address dense-mesh breakdown, a multiplicative Calderón preconditioner utilizing a modified static electric field integral operator is employed. Large-timestep breakdown and late-time instability are simultaneously resolved by rescaling the Helmholtz components leveraging the quasi-Helmholtz projectors and using temporal differentiation and integration as rescaling operators. This rescaling also balances the loop and star components at large timesteps, improving solution accuracy. The resulting discrete system is solved using a marching-on-in-time scheme and iterative solvers. Numerical experiments for simply- and multiply-connected dielectric scatterers, including highly non-smooth geometries, corroborate the accuracy, stability, and efficiency of the proposed approach.

**Index Terms**—Time-domain PMCHWT equation, late-time stabilization, preconditioning, quasi-Helmholtz projectors.

## I. INTRODUCTION

THE numerical computation of transient electromagnetic fields scattered by piecewise homogeneous dielectric bodies often relies on solving time-domain boundary integral equations. Among several formulations for dielectric scattering, the time-domain Poggio-Miller-Chang-Harrington-Wu-Tsai (TD-PMCHWT) equation [1] and the time-domain (TD)-Müller equation [2] are most widely used. The TD-PMCHWT equation, like the time-domain electric field integral equation (TD-EFIE) for perfect electric conductors, is a first-kind integral equation. In contrast, the TD-Müller equation, similar to the time-domain magnetic field integral equation (TD-MFIE), is of the second-kind. Despite its ill-conditioned nature, the TD-PMCHWT equation is more widely used in practice, as it generally yields more accurate numerical solutions than the TD-Müller formulation – see [3], [4] for supporting arguments in the frequency-domain. In this work, we focus on developing a numerical method for the TD-PMCHWT equation

Manuscript received April 19, 2005; revised August 26, 2008; accepted 19 May 2014. Date of publication 12 June 2014; date of current version 9 July 2014. This work was supported by European Research Council (ERC) under European Union’s Horizon 2020 Research and Innovation Program under Grant 101001847 and the Special Research Fund (BOF) of Ghent University under Grant BOFPDO.2024.0016.01. (Corresponding author: Van Chien Le.)

V. C. Le, C. Münger and K. Cools are with IDLab, Department of Information Technology at Ghent University - imec, 9000 Ghent, Belgium (e-mail: vanchien.le@ugent.be, cedric.muenger@ugent.be, kristof.cools@ugent.be).

F. P. Andriulli is with the Department of Electronics and Telecommunications, Politecnico di Torino, 10129 Turin, Italy (e-mail: francesco.andriulli@polito.it).

Color versions of one or more figures in this article are available at <https://doi.org/10.1109/>.

Digital Object Identifier 10.1109/.

that addresses three numerical challenges: ill-conditioning, late-time instability, and the loss of accuracy in the large-timestep regime. Here, the large-timestep regime refers to scenarios where relatively large timesteps are used in the time-domain simulation of the electromagnetic system. This regime resembles the low-frequency regime in the frequency-domain, since both are affected by similar numerical issues.

Due to its unbounded spectrum, the TD-PMCHWT operator produces ill-conditioned matrix systems upon discretization, particularly when the spatial mesh is dense or the timestep is large. These issues are commonly referred to as dense-mesh breakdown and large-timestep breakdown, respectively. In the dense-mesh regime, the accumulation of eigenvalues near zero and infinity causes the ill-conditioning. This breakdown can be effectively resolved through operator preconditioning [5], with Calderón-based techniques – built upon the Calderón identities – being especially prominent. Several such methods have been developed for the frequency-domain (FD-) PMCHWT equation [6]–[9], relying on either the PMCHWT operator itself or the electric field integral operator (EFIO) with a complex wavenumber. In the time-domain, frequency-domain operators with zero or purely imaginary wavenumbers can be used as preconditioners, avoiding complex-valued systems and suppressing interior resonances [10], [11]. Alternatively, the TD-PMCHWT operator itself, when appropriately discretized, can serve as a dense-mesh preconditioner [12]. However, using such a time-dependent operator requires an additional temporal discretization, leading to a more complicated marching-on-in-time (MOT) scheme.

Large-timestep breakdown, similar to low-frequency breakdown, stems from the opposite scaling behavior of matrix blocks associated with the loop and star components. While Calderón preconditioners can also be employed to address this issue in the frequency-domain – by exploiting the anti-commutative property of integral operators within the same medium [6] – this strategy becomes less effective in the time-domain setting. Specifically, the necessary Calderón anti-commutative relation does not hold between frequency-domain and time-domain operators, thus requiring nontrivial adaptations or dedicated implementation strategies. An alternative remedy is to rescale the Helmholtz blocks within the matrix system appropriately. This class of preconditioning has been extensively studied in the literature, both for frequency-domain formulations [13]–[17] and for their time-domain counterparts [11], [18]–[21].

In this work, we construct a diagonal dense-mesh preconditioner based on a modified static EFIO. The large-timestep

preconditioner, on the other hand, is derived from the loop-star decomposition via the quasi-Helmholtz projectors combined with an appropriate rescaling scheme. Constructing the dense-mesh and large-timestep preconditioners separately offers a key advantage: each preconditioner is tailored to address its specific breakdown regime while remaining stable and well-conditioned in the presence of the other. Consequently, their combination yields a simple yet effective strategy for mitigating both dense-mesh and large-timestep breakdowns.

In addition to ill-conditioning, the TD-PMCHWT equation is also notorious for its late-time instability, which manifests as non-decaying or even exponentially growing errors at late times [22]. This phenomenon superficially resembles direct-current instability of the TD-EFIE, but is considerably more sensitive to numerical quadrature errors [23]–[25]. Although various techniques can be used to suppress such errors [23], [26]–[30], these remedies generally do not guarantee stability, as they do not eliminate the underlying source of the instability. A recent comprehensive stability analysis of the TD-PMCHWT equation [31] identified the static solenoidal nullspace of the TD-EFIO as the principal cause of this instability. In this work, we eliminate this nullspace by adopting the rescaling scheme introduced in [20], which applies temporal differentiation and integration as rescaling factors associated with the Helmholtz components. This approach has been shown to stabilize time-domain solutions for both the TD-EFIE [18], [19] and TD-PMCHWT [20], [25], even under limited numerical precision in quadrature evaluations.

Lastly, at low frequencies or large timesteps, the solution to the PMCHWT equation suffers from unbalanced scaling between its loop and star components, which leads to a loss of significant digits in the dominated component when stored together with the dominant one in the same floating point variable [15], [32]–[34]. Even though the solution for the boundary fields may at first glance seem reasonable, large errors appear when computing secondary quantities of interest such as the far field. The accuracy loss can also be mitigated by means of the loop-star decomposition combined with a rescaling scheme [14], [15]. More specifically, when constructing the rescaling operators for the solution, we introduce a balancing factor to the dominated component, thereby defining a well-balanced auxiliary unknown that mitigates the numerical cancellation present in the original unknown.

In summary, this work addresses several numerical issues of the TD-PMCHWT equation, including dense-mesh breakdown, large-timestep breakdown, late-time instability, and the loss of solution accuracy at large timesteps. To combat dense-mesh breakdown, we introduce a multiplicative preconditioner utilizing a modified static EFIO. The remaining issues are simultaneously resolved by leveraging the loop-star decomposition combined with a rescaling scheme. The loop-star decomposition is performed via the quasi-Helmholtz projectors, which can be constructed without the need for costly identification of global loops [35]. The rescaling operators are applied to the loop and star components, with temporal differentiation and integration used as rescaling factors. The preconditioned and regularized formulation is temporally discretized using suitable pairs of trial and testing functions.

The resulting matrix system is efficiently solved using the MOT algorithm in combination with iterative solvers, yielding accurate and stable solutions. This paper extends our earlier conference contributions [18], [25] and the work in [24] by providing a rigorous analysis and a comprehensive suite of numerical results.

The structure of the paper is as follows. The next section gives an introduction to the TD-PMCHWT equation and its spatial Galerkin discretization. In Section III, we develop a dense-mesh preconditioner for the TD-PMCHWT formulation. Section IV is devoted to asymptotic large-timestep analysis and a regularization strategy for the preconditioned system. Section V discusses the temporal discretization and relevant implementation details. Several numerical results for both simply- and multiply-connected dielectric bodies including a highly non-smooth domain are presented in Section VI, corroborating the effectiveness of the proposed formulation. Finally, concluding remarks and future perspectives are provided in Section VII.

## II. TIME-DOMAIN PMCHWT EQUATION

Let  $\Gamma$  be the surface of an object in  $\mathbb{R}^3$  which is filled by a homogeneous dielectric material with permittivity  $\epsilon'$  and permeability  $\mu'$ . This object is immersed in a homogeneous background medium with permittivity  $\epsilon$  and permeability  $\mu$ . The surface  $\Gamma$  is assumed to be closed, connected, and orientable, with the outward unit normal  $\mathbf{n}$ . We consider the electromagnetic scattering of an incident transient plane wave  $(\mathbf{e}^{in}(\mathbf{x}, t), \mathbf{h}^{in}(\mathbf{x}, t))$  at the boundary  $\Gamma$ . The induced surface electric and magnetic current densities  $\mathbf{j}(\mathbf{x}, t)$  and  $\mathbf{m}(\mathbf{x}, t)$  are the solution to the following TD-PMCHWT equation<sup>1</sup>:

$$\begin{pmatrix} \eta\mathcal{T} + \eta'\mathcal{T}' & -\mathcal{K} - \mathcal{K}' \\ \mathcal{K} + \mathcal{K}' & \frac{1}{\eta}\mathcal{T} + \frac{1}{\eta'}\mathcal{T}' \end{pmatrix} \begin{pmatrix} \mathbf{j} \\ \mathbf{m} \end{pmatrix} = \begin{pmatrix} \mathbf{e}^{in} \times \mathbf{n} \\ \mathbf{h}^{in} \times \mathbf{n} \end{pmatrix}, \quad (1)$$

where the time-domain boundary integral operators  $\mathcal{T}$  and  $\mathcal{K}$  associated with the exterior region  $(\epsilon, \mu)$  are defined by

$$\begin{aligned} (\mathcal{T}\mathbf{j})(\mathbf{x}, t) &= (\mathcal{T}^s\mathbf{j})(\mathbf{x}, t) + (\mathcal{T}^h\mathbf{j})(\mathbf{x}, t), \\ (\mathcal{T}^s\mathbf{j})(\mathbf{x}, t) &= -\frac{1}{c} \mathbf{n} \times \int_{\Gamma} \frac{\partial_t \mathbf{j}(\mathbf{y}, \tau)}{4\pi |\mathbf{x} - \mathbf{y}|} d\mathbf{s}_{\mathbf{y}}, \\ (\mathcal{T}^h\mathbf{j})(\mathbf{x}, t) &= c \mathbf{n} \times \mathbf{grad}_{\mathbf{x}} \int_{\Gamma} \int_{-\infty}^{\tau} \frac{\operatorname{div}_{\Gamma} \mathbf{j}(\mathbf{y}, \xi)}{4\pi |\mathbf{x} - \mathbf{y}|} d\xi d\mathbf{s}_{\mathbf{y}}, \\ (\mathcal{K}\mathbf{j})(\mathbf{x}, t) &= \mathbf{n} \times p.v. \int_{\Gamma} \mathbf{curl}_{\mathbf{x}} \frac{\mathbf{j}(\mathbf{y}, \tau)}{4\pi |\mathbf{x} - \mathbf{y}|} d\mathbf{s}_{\mathbf{y}}. \end{aligned}$$

Here,  $\eta = \sqrt{\mu/\epsilon}$ ,  $c = 1/\sqrt{\mu\epsilon}$ , and  $\tau = t - |\mathbf{x} - \mathbf{y}|/c$ . The operators and quantities  $(\mathcal{T}', \mathcal{K}', \eta', \mu')$  associated with the interior region  $(\epsilon', \mu')$  are defined analogously. We note that the causality is imposed to ensure the uniqueness of a solution to (1), i.e.,  $\mathbf{j}(\mathbf{x}, t) = \mathbf{0}$  and  $\mathbf{m}(\mathbf{x}, t) = \mathbf{0}$  for all  $t < 0$  and  $\mathbf{x}$  in a neighborhood of  $\Gamma$ .

Let the boundary  $\Gamma$  be triangulated into a mesh of  $N_e$  edges,  $N_f$  triangles, and  $N_v$  vertices. We spatially discretize (1) using the Rao-Wilton-Glisson (RWG) basis functions  $\mathbf{f}_n(\mathbf{x})$ ,

<sup>1</sup>Time-domain continuous functions and operators are designated by calligraphic and normal symbols (e.g.,  $\mathcal{T}, \mathcal{K}, \mathbf{j}, \mathbf{m}, \mathbf{e}, \mathbf{h}$ ), while their semi-discrete and fully discrete counterparts are denoted by Fraktur (e.g.,  $\mathfrak{T}, \mathfrak{K}, \mathfrak{j}, \mathfrak{m}, \mathfrak{e}, \mathfrak{h}$ ) and upright Roman (e.g.,  $\mathbf{T}, \mathbf{K}, \mathbf{j}, \mathbf{m}, \mathbf{e}, \mathbf{h}$ ) letters, respectively.

with  $n = 1, 2, \dots, N_e$  [36]. The unknowns  $\mathbf{j}$  and  $\mathbf{m}$  are expanded in the RWG-spanned space, characterized by their time-dependent coefficient vectors

$$\begin{aligned}\mathbf{j}(t) &= (\mathbf{j}_1(t), \mathbf{j}_2(t), \dots, \mathbf{j}_{N_e}(t))^T, \\ \mathbf{m}(t) &= (\mathbf{m}_1(t), \mathbf{m}_2(t), \dots, \mathbf{m}_{N_e}(t))^T.\end{aligned}$$

By testing (1) with the rotated RWG functions  $\mathbf{n} \times \mathbf{f}_m(\mathbf{x})$ ,  $m = 1, 2, \dots, N_e$ , the vectors  $\mathbf{j}$  and  $\mathbf{m}$  are the solution to the following matrix system:

$$\begin{pmatrix} \mathfrak{Q}_{11} & \mathfrak{Q}_{12} \\ \mathfrak{Q}_{21} & \mathfrak{Q}_{22} \end{pmatrix} \begin{pmatrix} \mathbf{j}(t) \\ \mathbf{m}(t) \end{pmatrix} = \begin{pmatrix} \mathbf{e}(t) \\ \mathbf{h}(t) \end{pmatrix}, \quad (2)$$

where the block matrix is defined by

$$\mathfrak{Q} := \begin{pmatrix} \mathfrak{Q}_{11} & \mathfrak{Q}_{12} \\ \mathfrak{Q}_{21} & \mathfrak{Q}_{22} \end{pmatrix} = \begin{pmatrix} \eta \mathfrak{T} + \eta' \mathfrak{T}' & -\mathfrak{K} - \mathfrak{K}' \\ \mathfrak{K} + \mathfrak{K}' & \frac{1}{\eta} \mathfrak{T} + \frac{1}{\eta'} \mathfrak{T}' \end{pmatrix},$$

with the semi-discrete operators

$$\begin{aligned}\mathfrak{T} &= \mathfrak{T}^s + \mathfrak{T}^h, \\ [(\mathfrak{T}^s \mathbf{j})(t)]_m &= \sum_{n=1}^{N_e} \langle \mathbf{n} \times \mathbf{f}_m, \mathcal{T}^s(\mathbf{j}_n(t) \mathbf{f}_n) \rangle, \\ [(\mathfrak{T}^h \mathbf{j})(t)]_m &= \sum_{n=1}^{N_e} \langle \mathbf{n} \times \mathbf{f}_m, \mathcal{T}^h(\mathbf{j}_n(t) \mathbf{f}_n) \rangle, \\ [(\mathfrak{K} \mathbf{j})(t)]_m &= \sum_{n=1}^{N_e} \langle \mathbf{n} \times \mathbf{f}_m, \mathcal{K}(\mathbf{j}_n(t) \mathbf{f}_n) \rangle,\end{aligned}$$

and the  $\mathbf{L}^2(\Gamma)$ -inner product

$$\langle \mathbf{f}, \mathbf{g} \rangle = \int_{\Gamma} \mathbf{f}(\mathbf{x}) \cdot \mathbf{g}(\mathbf{x}) \, ds.$$

The operators  $\mathfrak{T}'$  and  $\mathfrak{K}'$  are defined analogously. The right-hand side vectors are given by

$$\begin{aligned}[\mathbf{e}(t)]_m &= \langle \mathbf{n} \times \mathbf{f}_m, \mathbf{e}^{in} \times \mathbf{n} \rangle, \\ [\mathbf{h}(t)]_m &= \langle \mathbf{n} \times \mathbf{f}_m, \mathbf{h}^{in} \times \mathbf{n} \rangle.\end{aligned}$$

Due to the unboundedness of the PMCHWT operator's spectrum, the semi-discrete system (2) produces ill-conditioned matrices when the surface mesh density increases [7]. In the next section, we propose a preconditioner to remedy this dense-mesh breakdown.

### III. DENSE-MESH PRECONDITIONING

We involve the following “static EFIO” in constructing a dense-mesh preconditioner:

$$T_0 = T_0^s + T_0^h, \quad (3)$$

where the singular and hyper-singular parts are defined by

$$\begin{aligned}(T_0^s \mathbf{j})(\mathbf{x}) &= \frac{1}{D} \mathbf{n} \times \int_{\Gamma} \frac{\mathbf{j}(\mathbf{y})}{4\pi |\mathbf{x} - \mathbf{y}|} \, ds_{\mathbf{y}}, \\ (T_0^h \mathbf{j})(\mathbf{x}) &= -D \mathbf{n} \times \mathbf{grad}_{\mathbf{x}} \int_{\Gamma} \frac{\operatorname{div}_{\Gamma} \mathbf{j}(\mathbf{y})}{4\pi |\mathbf{x} - \mathbf{y}|} \, ds_{\mathbf{y}}.\end{aligned}$$

The scatterer diameter  $D$  of length unit is included to ensure dimensional consistency between  $T_0^s$  and  $T_0^h$ . The operator  $T_0$  is symmetric and elliptic on the energy trace space

$\mathbf{H}_x^{-1/2}(\operatorname{div}_{\Gamma}, \Gamma)$  [37], yielding symmetric positive-definite matrices when discretized using a Galerkin scheme. In particular,  $T_0$  is discretized using the Buffa-Christiansen (BC) basis functions  $\mathbf{g}_n(\mathbf{x})$ ,  $n = 1, 2, \dots, N_e$ , [38] as follows:

$$\begin{aligned}\mathbb{T}_0 &= \mathbb{T}_0^s + \mathbb{T}_0^h, \\ [\mathbb{T}_0^s]_{mn} &= \langle \mathbf{n} \times \mathbf{g}_m, T_0^s \mathbf{g}_n \rangle, \\ [\mathbb{T}_0^h]_{mn} &= \langle \mathbf{n} \times \mathbf{g}_m, T_0^h \mathbf{g}_n \rangle.\end{aligned}$$

Next, we develop a diagonal version of  $\mathbb{T}_0$  with respect to the loop-star basis. The loop-star diagonal structure will benefit our large-timestep regularization in the next section. To do so, we recall the Helmholtz decomposition (the so-called Hodge decomposition for boundary trace functions)

$$\mathbf{H}_x^{-1/2}(\operatorname{div}_{\Gamma}, \Gamma) = \mathbf{X}_{\Gamma} \oplus \mathbf{H}_x^{-1/2}(\operatorname{div}_{\Gamma} 0, \Gamma),$$

where  $\mathbf{X}_{\Gamma}$  and  $\mathbf{H}_x^{-1/2}(\operatorname{div}_{\Gamma} 0, \Gamma)$  are the subspaces of irrotational (star) and solenoidal (loop) functions, respectively [39], [40]. In the discrete space spanned by the BC basis functions, the quasi-Helmholtz projectors  $\mathbb{P}^{\Lambda}$  and  $\mathbb{P}^{\Sigma H}$  can approximate the Helmholtz decomposition. Roughly speaking, they map from the BC space onto its star and loop subspaces, respectively (see [13] and also Section IV for more details). Moreover, they are  $l^2$ -orthogonal, i.e.,  $\mathbb{P}^{\Sigma H} \mathbb{P}^{\Lambda} = \mathbf{0}$ . In this paper, we consider the following loop-star diagonal dense-mesh preconditioner:

$$\mathbb{T} = \mathbb{T}^{\Sigma H} + \mathbb{T}^{\Lambda} := \mathbb{P}^{\Sigma H} \mathbb{T}_0^s \mathbb{P}^{\Sigma H} + \mathbb{P}^{\Lambda} \mathbb{T}_0^h \mathbb{P}^{\Lambda}. \quad (4)$$

This matrix is also symmetric and positive-definite, like  $\mathbb{T}_0$ . According to the coercivity of the PMCHWT equation in [41] and the general recipe in [5],  $\mathbb{T}$  can play the role of a dense-mesh preconditioner to the semi-discrete system (2). The preconditioning is supplemented with the Gram matrix

$$[\mathbf{G}]_{mn} = \langle \mathbf{n} \times \mathbf{f}_m, \mathbf{g}_n \rangle.$$

Thus, the dense-mesh preconditioned version of (2) reads

$$\mathbb{T} \mathbf{G}^{-1} \begin{pmatrix} \mathfrak{Q}_{11} & \mathfrak{Q}_{12} \\ \mathfrak{Q}_{21} & \mathfrak{Q}_{22} \end{pmatrix} \begin{pmatrix} \mathbf{j}(t) \\ \mathbf{m}(t) \end{pmatrix} = \mathbb{T} \mathbf{G}^{-1} \begin{pmatrix} \mathbf{e}(t) \\ \mathbf{h}(t) \end{pmatrix}. \quad (5)$$

Here and throughout the paper, multiplication of a block matrix with block-sized matrices is understood as block-wise multiplication. The system (5) (when accompanied by  $\mathbf{G}^{-T}$ ) produces well-conditioned matrices regardless of the mesh refinement and the basis chosen for the finite element space [5]. The preconditioner  $\mathbb{T}$  is not only effective in bounding the condition number of the linear system with respect to the mesh density, but also immune to other numerical issues, such as the large-timestep breakdown, the loss of solution accuracy at large timesteps, as well as the resonant instability.

We remark here that the static operator  $T_0$  can be replaced by any EFIO  $T_{-\iota\kappa}$  of a fixed imaginary wavenumber  $-\iota\kappa$ , with  $\kappa > 0$  [42]. In addition, as the matrix  $\mathbb{T}$  is diagonal in the loop-star basis, one can change the sign of the hyper-singular part  $\mathbb{P}^{\Lambda} \mathbb{T}_0^h \mathbb{P}^{\Lambda}$  in (4) without losing the invertibility. The resulting matrix  $\tilde{\mathbb{T}}$  coincides (up to some factors) with the low-frequency limit of the quasi-Helmholtz projected (qHP) EFIO in [18] (with the RWG basis replaced by the BC basis).  $\tilde{\mathbb{T}}$  is also a dense-mesh preconditioner to (2). Moreover, the system (2)

preconditioned by  $\tilde{\mathbb{T}}$  has the same bound of condition numbers as (5), since  $\mathbb{T}$  and  $\tilde{\mathbb{T}}$  share the norm and the coercivity constant.

The formulation (5) is well-conditioned when the mesh size decreases. However, it is still time-dependent, necessitating a discretization in time. In addition, its temporal discretization will suffer from large-timestep breakdown, late-time instability, and the loss of solution accuracy at large timesteps.

#### IV. LARGE-TIMESTEP REGULARIZATION

This section presents an analysis on the asymptotic large-timestep scaling behavior of the dense-mesh preconditioned formulation (5). The goal is to investigate the mechanisms underlying large-timestep breakdown and the loss of solution accuracy at large timesteps. Based on these insights, we propose a regularization strategy that simultaneously eliminates large-timestep ill-conditioning, late-time instability, and the loss of accuracy.

To that end, we assume that the loop-star decomposition is employed, resulting in the transformation matrices  $\Lambda$ ,  $\mathbf{H}$ , and  $\Sigma$  that respectively map local loops, global loops (quasi-harmonic functions), and stars to discrete functions. Particularly in the context of the RWG basis, the matrix  $\Lambda \in \mathbb{R}^{N_e \times N_v}$  is constructed via the node-edge adjacency information as

$$[\Lambda]_{mn} := \begin{cases} 1 & \text{if the vertex } n \text{ is identical with } v_m^+, \\ -1 & \text{if the vertex } n \text{ is identical with } v_m^-, \\ 0 & \text{otherwise,} \end{cases}$$

where the edge  $e_m$ ,  $m = 1, 2, \dots, N_e$ , is oriented from the vertex  $v_m^-$  to  $v_m^+$ . The matrix  $\Sigma \in \mathbb{R}^{N_e \times N_f}$  is linked to face-edge connectivity as follows:

$$[\Sigma]_{mn} := \begin{cases} 1 & \text{if the triangle } n \text{ is identical with } c_m^+, \\ -1 & \text{if the triangle } n \text{ is identical with } c_m^-, \\ 0 & \text{otherwise,} \end{cases}$$

where the RWG basis function  $f_m(\mathbf{x})$ ,  $m = 1, 2, \dots, N_e$ , represents a current flowing from the triangle  $c_m^+$  to  $c_m^-$  [35].

Both the local loops and the global loops represent solenoidal functions. When the surface  $\Gamma$  is simply-connected, the matrix  $\mathbf{H} = \emptyset$ . We emphasize that  $\mathbf{H}$  is introduced for the analysis purpose only. In our numerical scheme, the costly explicit identification of  $\mathbf{H}$  is not required. Throughout this section, the large-timestep scaling of vector fields and matrices is with respect to the basis  $(\Lambda \ \mathbf{H} \ \Sigma)^\top$ .

##### A. Large-Timestep Scaling

The large-timestep scaling of quantities and matrices in the time-domain is similar to their low-frequency counterparts in the frequency-domain setting. For consistency between time-domain and frequency-domain, we use the notation  $\omega := \Delta t^{-1}$  in further large-timestep analysis, where  $\Delta t$  denotes the timestep used in the simulation. In the large-timestep regime, the plane-wave excitation and its induced surface current densities scale as follows [14], [15], [32]:

$$\begin{aligned} \mathbf{e} &\sim \mathbf{h} = \mathcal{O}(\omega, \omega, 1)^\top, \\ \mathbf{j} &\sim \mathbf{m} = \mathcal{O}(1, \omega, \omega)^\top. \end{aligned}$$

When  $\omega \rightarrow 0$  (equivalently,  $\Delta t \rightarrow \infty$ ), the unknowns  $\mathbf{j}$  and  $\mathbf{m}$  are dominated by their local loop components. As a consequence, the global loops and stars suffer from a loss of significant digits when stored together with the local loops in the same floating point variable. This numerical loss of accuracy may not manifest itself in the solution or in the induced near fields, but it will be prominently present in the far-field computation [11]. The TD-PMCHWT matrix  $\mathfrak{Q}$  in (2) has the following large-timestep scaling:

$$\begin{pmatrix} \mathfrak{Q}_{11} & \mathfrak{Q}_{12} \\ \mathfrak{Q}_{21} & \mathfrak{Q}_{22} \end{pmatrix} = \mathcal{O} \left( \begin{array}{ccc|ccc} \omega & \omega & \omega & \omega^2 & \omega^2 & 1 \\ \omega & \omega & \omega & \omega^2 & 1 & 1 \\ \omega & \omega & \omega^{-1} & 1 & 1 & 1 \\ \hline \omega^2 & \omega^2 & 1 & \omega & \omega & \omega \\ \omega^2 & 1 & 1 & \omega & \omega & \omega \\ 1 & 1 & 1 & \omega & \omega & \omega^{-1} \end{array} \right).$$

This scaling can be derived from the large-timestep scaling of the TD-EFIE and TD-MFIE operators [11], or from the low-frequency counterpart in the frequency-domain [14], [15]. The opposite scaling behaviors  $\mathcal{O}(\omega)$  and  $\mathcal{O}(\omega^{-1})$  in the diagonal blocks stemming from the temporal differentiation and integration in the TD-EFIOs are the origin of large-timestep breakdown. More specifically, the condition number of  $\mathfrak{Q}$  grows as  $\mathcal{O}(\omega^{-1})/\mathcal{O}(\omega) = \mathcal{O}(\omega^{-2})$  when  $\omega \rightarrow 0$ .

Next, we derive the large-timestep scaling of the dense-mesh preconditioned formulation (5). Note that the dense-mesh preconditioner  $\mathbb{T}$  and the Gram matrix  $\mathbf{G}$  are independent of timestep  $\Delta t$ . In addition, in the BC basis (used for discretizing  $\mathbb{T}$  and  $\mathbf{G}$ ), the role of  $\Lambda$  and  $\Sigma$  are exchanged (i.e.,  $\Lambda$  represents the stars and  $\Sigma$  represents the local loops), while  $\mathbf{H}$  still represents the global loops [13]. Due to its diagonal structure,  $\mathbb{T}$  behaves as follows in the basis  $(\Lambda \ \mathbf{H} \ \Sigma)^\top$ :

$$\mathbb{T} = \begin{pmatrix} \square & 0 & 0 \\ 0 & \square & \square \\ 0 & \square & \square \end{pmatrix},$$

where  $\square$  indicates a non-zero block. According to [19], the inverse Gram matrix  $\mathbf{G}^{-1}$  has the following structure:

$$\mathbf{G}^{-1} = \begin{pmatrix} \square & 0 & 0 \\ \square & \square & 0 \\ \square & \square & \square \end{pmatrix}.$$

Combining the large-timestep scaling and algebraic structure of vectors and matrices, the large-timestep scaling of the formulation (5) reads as follows:

$$\begin{pmatrix} \omega & \omega & \omega & \omega^2 & \omega^2 & 1 \\ \omega & \omega & \omega^{-1} & 1 & 1 & 1 \\ \omega & \omega & \omega^{-1} & 1 & 1 & 1 \\ \hline \omega^2 & \omega^2 & 1 & \omega & \omega & \omega \\ 1 & 1 & 1 & \omega & \omega & \omega^{-1} \\ 1 & 1 & 1 & \omega & \omega & \omega^{-1} \end{pmatrix} \begin{pmatrix} 1 \\ \omega \\ \omega \\ 1 \\ \omega \\ \omega \end{pmatrix} = \begin{pmatrix} \omega \\ 1 \\ 1 \\ \omega \\ 1 \\ 1 \end{pmatrix}. \quad (6)$$

It is convincing that (5) still suffers from both large-timestep breakdown and the loss of solution accuracy. In the following section, a regularization for (5) is introduced, based on its large-timestep scaling behavior in (6).

### B. Large-Timestep Regularization

We recall the quasi-Helmholtz projectors associated with the RWG and BC bases

$$\begin{aligned}\mathbf{P}^\Sigma &:= \Sigma(\Sigma^\top \Sigma)^+ \Sigma^\top, & \mathbf{P}^{\Lambda H} &:= I - \mathbf{P}^\Sigma, \\ \mathbb{P}^\Lambda &:= \Lambda(\Lambda^\top \Lambda)^+ \Lambda^\top, & \mathbb{P}^{\Sigma H} &:= I - \mathbb{P}^\Lambda,\end{aligned}$$

where the subscript  $+$  indicates the Moore–Penrose pseudo-inverse and  $I$  is the identity matrix of size  $N_e$  [13]. Approximately speaking,  $\mathbf{P}^{\Lambda H}$  and  $\mathbf{P}^\Sigma$  are respectively the projectors from the RWG space into its loop and star subspaces. Similarly,  $\mathbb{P}^{\Sigma H}$  and  $\mathbb{P}^\Lambda$  are the corresponding projectors associated with the BC space. Notably, these constructions of the loop-star decomposition do not require the costly explicit identification of the global loops  $\mathbf{H}$ . The drawback is that the local and global loops are not distinguished. However, we will demonstrate in further analysis this is unproblematic.

Using the quasi-Helmholtz projectors, we now propose a large-timestep regularization for (5). In order to mitigate the imbalance between the components of the solution  $\mathbf{j}$  and  $\mathbf{m}$ , we introduce the right rescaling operator

$$\mathbf{R} := \mathbf{P}^{\Lambda H} + \alpha \mathbf{P}^\Sigma, \quad (7)$$

where the dimensionless factor  $\alpha = \mathcal{O}(\omega)$  is specified later. Obviously, the operator  $\mathbf{R}$  is invertible and its inverse is given

$$\mathbf{R}^{-1} = \mathbf{P}^{\Lambda H} + \alpha^{-1} \mathbf{P}^\Sigma.$$

Next, we rescale the unknowns  $\mathbf{j}$  and  $\mathbf{m}$  by  $\mathbf{R}^{-1}$ , giving rise to the two auxiliary unknowns

$$\mathbf{u}(t) := \mathbf{R}^{-1} \mathbf{j}(t), \quad \mathbf{v}(t) := \mathbf{R}^{-1} \mathbf{m}(t), \quad (8)$$

which scale as follows when  $\omega \rightarrow 0$ :

$$\mathbf{u} \sim \mathbf{v} = \mathcal{O}(1, \omega, 1)^\top.$$

It is noticed that, in  $\mathbf{u}$  and  $\mathbf{v}$ , the global loops  $\mathbf{H}$  remain dominated by the local loops and the stars. Although  $\mathbf{H}$  has a fixed rank, this imbalance still causes numerical cancellation. Nevertheless, this cancellation is not problematic for the computation of the scattered fields, since the contribution of  $\mathbf{H}$  is only of order  $\mathcal{O}(\omega)$  relative to that of  $\mathbf{A}$ . Moreover, this behavior is physical, as a plane wave does not excite global loop currents in the static limit [14]. Other types of excitation may lead to a complete balance among the three components of the rescaled unknowns. Further details on the low-frequency scaling behavior of different excitations can be found in [43].

By introducing the rescaling operator  $\mathbf{R}$ , one can transform an equation of the physical unknowns  $\mathbf{j}$  and  $\mathbf{m}$  to another equation of the auxiliary unknowns  $\mathbf{u}$  and  $\mathbf{v}$ , thereby significantly mitigating the imbalance in the solution and hence improving the accuracy at large timesteps. The physical currents  $\mathbf{j}$  and  $\mathbf{m}$  can be obtained back by simply applying  $\mathbf{R}$  to  $\mathbf{u}$  and  $\mathbf{v}$ , i.e.,

$$\mathbf{j}(t) = \mathbf{R} \mathbf{u}(t), \quad \mathbf{m}(t) = \mathbf{R} \mathbf{v}(t). \quad (9)$$

The operator  $\mathbf{R}$  is called the right rescaling operator because it is multiplied on the right of the TD-PMCHWT matrix. To eliminate the large-timestep ill-conditioning of (5), we also need the following left rescaling operator:

$$\mathbb{L} := \mathbb{P}^{\Sigma H} + \alpha^{-1} \mathbb{P}^\Lambda. \quad (10)$$

This operator is built on the quasi-Helmholtz projectors  $\mathbb{P}^{\Sigma H}$  and  $\mathbb{P}^\Lambda$  associated with the BC space, as (5) defines a linear map from the RWG space into the dual of the BC space. Now, applying  $\mathbb{L}$  to (5) and substituting the unknowns  $\mathbf{j}$  and  $\mathbf{m}$  by (9), we end up with the following formulation of the auxiliary unknowns  $\mathbf{u}$  and  $\mathbf{v}$ :

$$\begin{pmatrix} \tilde{\mathfrak{Q}}_{11} & \tilde{\mathfrak{Q}}_{12} \\ \tilde{\mathfrak{Q}}_{21} & \tilde{\mathfrak{Q}}_{22} \end{pmatrix} \begin{pmatrix} \mathbf{u}(t) \\ \mathbf{v}(t) \end{pmatrix} = \begin{pmatrix} \tilde{\mathbf{e}}(t) \\ \tilde{\mathbf{h}}(t) \end{pmatrix}, \quad (11)$$

where the matrix blocks

$$\tilde{\mathfrak{Q}}_{ij} = \mathbb{L} \mathbb{T} \mathbf{G}^{-1} \mathfrak{Q}_{ij} \mathbf{R},$$

with  $i, j = 1, 2$ , and the right-hand side

$$\tilde{\mathbf{e}} = \mathbb{L} \mathbb{T} \mathbf{G}^{-1} \mathbf{e}, \quad \tilde{\mathbf{h}} = \mathbb{L} \mathbb{T} \mathbf{G}^{-1} \mathbf{h}.$$

By some simple calculations, one can determine the large-timestep scaling of (11) as follows:

$$\begin{pmatrix} 1 & 1 & \omega & \omega & \omega & 1 \\ \omega & \omega & 1 & 1 & 1 & \omega \\ \omega & \omega & 1 & 1 & 1 & \omega \\ \hline \omega & \omega & 1 & 1 & 1 & \omega \\ 1 & 1 & \omega & \omega & \omega & 1 \\ 1 & 1 & \omega & \omega & \omega & 1 \end{pmatrix} \begin{pmatrix} 1 \\ \omega \\ 1 \\ 1 \\ \omega \\ 1 \end{pmatrix} = \begin{pmatrix} 1 \\ 1 \\ 1 \\ 1 \\ 1 \\ 1 \end{pmatrix}.$$

Apparently, there is no factor  $\mathcal{O}(\omega^{-1})$  in the scaling of the square matrix in (11). Numerical experiments further indicate that its condition number remains bounded as  $\omega \rightarrow 0$ . Consequently, the regularized formulation (11) is free from large-timestep breakdown, and its solution is well-balanced when the timestep  $\Delta t$  is large.

The left and right rescaling operators  $\mathbb{L}$  and  $\mathbf{R}$  are essential in developing (11). These operators differ from those proposed for the FD-PMCHWT formulation in [14], as we do not require the symmetry between the two components. However, their effectiveness remains the same as those in [14], as long as  $\alpha = \mathcal{O}(\omega)$ . In the time-domain setting, there are two possible choices of  $\alpha$  satisfying this criterion, either  $\alpha = T_{\max} \Delta t^{-1}$  or  $\alpha = T_{\max} \partial_t$ , where the constant  $T_{\max}$  of time unit is included to render  $\alpha$  dimensionless [11]. The latter option comes from the fact that for a very slowly varying function, the time derivative is of order of  $\Delta t^{-1}$  even when  $\Delta t$  is relatively large (as can be seen from a Taylor expansion). Please note that if we are solely concerned with conditioning and the loss of accuracy – direct counterparts of the challenges present in the frequency-domain – then either choice suffices. In the next section, time-domain specific problems will prompt us to reconsider this design choice.

It is worth noting that the left rescaling operator  $\mathbb{L}$  and the dense-mesh preconditioner  $\mathbb{T}$  are commuting due to the loop-star diagonal structure of  $\mathbb{T}$ , i.e.,

$$\mathbb{L} \mathbb{T} = \mathbb{T} \mathbb{L} = \mathbb{P}^{\Sigma H} \mathbb{T}_0^s \mathbb{P}^{\Sigma H} + \alpha^{-1} \mathbb{P}^\Lambda \mathbb{T}_0^h \mathbb{P}^\Lambda.$$

Therefore, their positions in (11) can be interchanged, leading to a dense-mesh preconditioned version (by  $\mathbb{T}$ ) of the large-timestep regularized TD-PMCHWT formulation in [20]. The preconditioned and regularized formulation (11) is different from the one proposed in [24], where the author preconditioned the regularized TD-PMCHWT system by its dual counterpart.

### C. Late-Time Stabilization

Up to now, we have eliminated three out of four numerical issues of the TD-PMCHWT formulation: dense-mesh breakdown, large-timestep breakdown, and the loss of solution accuracy at large timesteps. This section discusses a remedy to late-time instability, which was identified as originating from the well-known nullspace of the TD-EFIOs comprising all constant-in-time solenoidal functions [31].

Our remedy is to get rid of the nullspace of the TD-EFIOs, by choosing an appropriate rescaling factor  $\alpha$  in (7) and (10). More specifically, we set

$$\alpha = \tilde{\partial}_t := T_{\max} \partial_t, \quad \alpha^{-1} = \tilde{\partial}_t^{-1} := \partial_t^{-1} / T_{\max}, \quad (12)$$

where  $\partial_t^{-1}$  is the temporal integration over  $(-\infty, t)$  and  $T_{\max} = D/c_{\min}$ , with  $c_{\min} := \min(c, c')$ . The idea of choosing temporal differentiation and integration as the rescaling factors has been introduced in [18], [19] for the TD-EFIE. In the following, we demonstrate how to adapt that approach to the TD-PMCHWT equation. Please note that the low-frequency regularization of the PMCHWT is different from that of the EFIE. In particular, the left rescaling operator of the EFIE is applied on the RWG dual space (as the EFIE is tested by the RWG basis functions) [18], whereas that of the PMCHWT acts on the BC spaces. The necessity of using a different regularization scheme for the PMCHWT equation has been explained in [14].

Considering the diagonal blocks  $\tilde{\mathfrak{Q}}_{11}$  and  $\tilde{\mathfrak{Q}}_{22}$  in (11) that contain the TD-EFIOs  $\mathcal{T}$  and  $\mathcal{T}'$ , with a particular attention to the contributions from  $\mathcal{T}$  (as  $\mathcal{T}'$  can be handled analogously), we have the decomposition

$$\mathfrak{Z} := \mathbb{L} \mathbb{T} \mathbf{G}^{-1} \mathfrak{T} \mathbf{R} = \mathfrak{Z}_{ll} + \mathfrak{Z}_{ls} + \mathfrak{Z}_{sl} + \mathfrak{Z}_{ss}, \quad (13)$$

where

$$\begin{aligned} \mathfrak{Z}_{ll} &:= \mathbb{T}^{\Sigma H} \mathbf{G}^{-1} \mathfrak{T}^s \mathbf{P}^{\Lambda H}, \\ \mathfrak{Z}_{ls} &:= \mathbb{T}^{\Sigma H} \mathbf{G}^{-1} \tilde{\partial}_t \mathfrak{T} \mathbf{P}^{\Sigma}, \\ \mathfrak{Z}_{sl} &:= \mathbb{T}^{\Lambda} \mathbf{G}^{-1} \mathbf{P}^{\Lambda H} \tilde{\partial}_t^{-1} \mathfrak{T}^s \mathbf{P}^{\Lambda H}, \\ \mathfrak{Z}_{ss} &:= \mathbb{T}^{\Lambda} \mathbf{G}^{-1} \mathbf{P}^{\Lambda H} \mathfrak{T}^s \mathbf{P}^{\Sigma}. \end{aligned}$$

Here, we took into account the fact  $\mathbf{P}^{\Lambda H} \mathfrak{T}^h = \mathfrak{T}^h \mathbf{P}^{\Lambda H} = \mathbf{0}$ . The projector  $\mathbf{P}^{\Lambda H}$  appears in the middle of the last two terms because we leveraged the identity  $\mathbb{P}^{\Lambda} \mathbf{G}^{-1} \mathbf{P}^{\Sigma} = \mathbf{0}$  from [19], thereby getting rid of the contributions from the hyper-singular term  $\mathfrak{T}^h$ . One can see that the rescaling temporal operators  $\tilde{\partial}_t$  and  $\tilde{\partial}_t^{-1}$  only come into play in the components  $\mathfrak{Z}_{ls}$  and  $\mathfrak{Z}_{sl}$ . In particular,  $\tilde{\partial}_t^{-1}$  cancels the temporal differentiation in  $\mathfrak{T}^s$ . Consequently, the kernel of  $\mathfrak{Z}_{sl}$  does not contain any non-zero constant-in-time solenoidal functions, hence, neither does  $\mathfrak{Z}$ 's. More precisely,  $\mathfrak{Z}$  only has a trivial nullspace. The operator  $\tilde{\partial}_t$  also cancels out the temporal integration in  $\mathfrak{T}^h$ , whose benefit will be clarified in the next section.

To conclude this section, the preconditioned and regularized formulation (11), with  $\alpha$  chosen in (12), is immune to ill-conditioning, late-time instability, and the loss of accuracy at large timesteps. Since (11) is still time-dependent, a temporal discretization scheme is needed.

## V. DISCRETIZATION AND IMPLEMENTATION

### A. Temporal Discretization

This section presents a temporal discretization of the regularized TD-PMCHWT formulation (11). When introducing the new unknowns  $\mathbf{u}$  and  $\mathbf{v}$ , we have added a temporal integration  $\tilde{\partial}_t^{-1}$  to the stars  $\mathbf{P}^{\Sigma}$  of  $\mathbf{j}$  and  $\mathbf{m}$ , while retained their loops  $\mathbf{P}^{\Lambda H}$ . To guarantee the compatibility of the two components of  $\mathbf{j}$  and  $\mathbf{m}$  (physical unknowns), we shall discretize the stars and loops of  $\mathbf{u}$  and  $\mathbf{v}$  by two different sets of temporal basis functions, such that the set for the stars  $\mathbf{P}^{\Sigma}$  is of one order higher than the set for the loops  $\mathbf{P}^{\Lambda H}$ . In this paper, we opt for the lowest-order pair for simplicity.

Let  $N_t$  be the number of timesteps we want to compute for the numerical solution. The auxiliary unknowns  $\mathbf{u}$  and  $\mathbf{v}$  are approximated as follows:

$$\begin{pmatrix} \mathbf{u}(t) \\ \mathbf{v}(t) \end{pmatrix} = \sum_{i=1}^{N_t} \left( p_i(t) \mathbf{P}^{\Lambda H} + h_i(t) \mathbf{P}^{\Sigma} \right) \begin{pmatrix} \mathbf{u}_i \\ \mathbf{v}_i \end{pmatrix},$$

where the two sets of temporal shifted basis functions

$$\begin{aligned} p_i(t) &:= p_0(t - i\Delta t), & p_0(t) &= \begin{cases} 1 & -\Delta t < t < 0, \\ 0 & \text{otherwise,} \end{cases} \\ h_i(t) &:= h_0(t - i\Delta t), & h_0(t) &= \begin{cases} 1 - \frac{|t|}{\Delta t} & |t| \leq \Delta t, \\ 0 & \text{otherwise,} \end{cases} \end{aligned}$$

with  $i = 1, 2, \dots, N_t$ . For the testing, a similar argument applies, with a note that the star component  $\mathbb{P}^{\Lambda}$  in (10) contains an extra temporal integration due to the rescaling. This, together with the compatibility property

$$\frac{1}{\Delta t} \int_{\mathbb{R}} p_i(t) p_0(t + \xi) dt = \int_{\mathbb{R}} \delta_i(t) h_0(t + \xi) dt, \quad (14)$$

which holds for all  $\xi \in \mathbb{R}$  and  $i = 0, 1, \dots, N_t$ , leads to the testing functions  $\frac{1}{\Delta t} p_k(t) \mathbb{P}^{\Sigma H} + \delta_k(t) \mathbb{P}^{\Lambda}$ , with  $\delta_k(t) := \delta(t - k\Delta t)$  the Dirac delta distributions and  $k = 1, 2, \dots, N_t$ . Denoting  $\mathbf{w}_i := (\mathbf{u}_i, \mathbf{v}_i)^T$ , the temporal testing of (11) yields a lower triangular block matrix system of the form

$$\begin{pmatrix} \mathbf{Q}_0 & & & \\ \mathbf{Q}_1 & \mathbf{Q}_0 & & \\ \vdots & \vdots & \ddots & \\ \mathbf{Q}_{N_t-1} & \mathbf{Q}_{N_t-2} & \dots & \mathbf{Q}_0 \end{pmatrix} \begin{pmatrix} \mathbf{w}_1 \\ \mathbf{w}_2 \\ \vdots \\ \mathbf{w}_{N_t} \end{pmatrix} = \begin{pmatrix} \mathbf{r}_1 \\ \mathbf{r}_2 \\ \vdots \\ \mathbf{r}_{N_t} \end{pmatrix}. \quad (15)$$

Please note that this temporal discretization is highly non-standard, since the basis functions do not even possess a tensorial structure. In the following sections, we will compute the matrix blocks  $\mathbf{Q}_k$ , with  $k = 0, 1, \dots, N_t - 1$ , and the right-hand side vectors  $\mathbf{r}_i, i = 1, 2, \dots, N_t$ , using a more conventional scheme. Once the matrix and the right-hand side are computed, the unknowns  $\mathbf{w}_i, i = 1, 2, \dots, N_t$ , can be sequentially obtained by solving the MOT equation

$$\mathbf{Q}_0 \mathbf{w}_i = \mathbf{r}_i - \sum_{k=1}^{i-1} \mathbf{Q}_k \mathbf{w}_{i-k}. \quad (16)$$

This equation can be efficiently solved by iterative solvers (e.g., GMRES solvers), since the matrix  $\mathbf{Q}_0$  is well-conditioned when the spatial mesh size decreases or the timestep increases, as the result of preconditioning.

After solving the fully discrete system (15) for the auxiliary unknowns, a post-processing procedure is performed to obtain the physical current densities. Let  $(\mathbf{j}_i, \mathbf{m}_i)^\top$  be the expansion coefficient of  $(\mathbf{j}(t), \mathbf{m}(t))^\top$  corresponding to the temporal basis function  $p_i(t)$ , with  $i = 1, 2, \dots, N_t$ . Following [11], we can deduce that

$$\begin{pmatrix} \mathbf{j}_i \\ \mathbf{m}_i \end{pmatrix} = \mathbf{P}^{\Lambda H} \begin{pmatrix} \mathbf{u}_i \\ \mathbf{v}_i \end{pmatrix} + \frac{T_{\max}}{\Delta t} \mathbf{P}^\Sigma \begin{pmatrix} \mathbf{u}_i - \mathbf{u}_{i-1} \\ \mathbf{v}_i - \mathbf{v}_{i-1} \end{pmatrix}, \quad (17)$$

with the convention  $\mathbf{u}_0 = \mathbf{v}_0 = \mathbf{0}$ . In fact, the numerical solution computed from (17) still suffers from the loss of accuracy as the star component is dominated when  $\Delta t \rightarrow \infty$ . In the far-field computation, the two components  $\mathbf{P}^{\Lambda H}$  and  $\mathbf{P}^\Sigma$  of  $\mathbf{j}_i$  and  $\mathbf{m}_i$  should be stored separately to avoid the loss of significant digits.

### B. Computation of Matrix Blocks

In this section, we describe in detail how to compute the matrix blocks  $\mathbf{Q}_i$  in (15). First, we introduce the following continuously differentiable piecewise-quadratic function:

$$q_0(t) := \frac{1}{\Delta t} \int_{\mathbb{R}} p_0(\xi) h_0(t + \xi) d\xi$$

$$= \begin{cases} \frac{1}{2} \left( \frac{t}{\Delta t} + 1 \right)^2 & -\Delta t \leq t < 0, \\ \frac{1}{2} - \frac{t^2}{\Delta t^2} + \frac{t}{\Delta t} & 0 \leq t < \Delta t, \\ \frac{1}{2} \left( \frac{t}{\Delta t} - 2 \right)^2 & \Delta t \leq t \leq 2\Delta t, \\ 0 & \text{otherwise.} \end{cases}$$

This function also satisfies the compatibility

$$\frac{1}{\Delta t} \int_{\mathbb{R}} p_i(t) h_0(t + \xi) dt = \int_{\mathbb{R}} \delta_i(t) q_0(t + \xi) dt. \quad (18)$$

Next, the matrix blocks  $\mathbf{Q}_i$  in (15) are defined by

$$\mathbf{Q}_i = \int_{\mathbb{R}} \left( \frac{p_i(t)}{\Delta t} \mathbb{P}^{\Sigma H} + \delta_i(t) \mathbb{P}^\Lambda \right) \tilde{\mathfrak{Q}} \left( p_0(t) \mathbf{P}^{\Lambda H} + h_0(t) \mathbf{P}^\Sigma \right) dt,$$

with  $i = 0, 1, \dots, N_t - 1$ , and  $\tilde{\mathfrak{Q}}$  the block matrix in (11), i.e.,

$$\tilde{\mathfrak{Q}} = \begin{pmatrix} \tilde{\mathfrak{Q}}_{11} & \tilde{\mathfrak{Q}}_{12} \\ \tilde{\mathfrak{Q}}_{21} & \tilde{\mathfrak{Q}}_{22} \end{pmatrix}.$$

Analogous to (13),  $\mathbf{Q}_i$  can be decomposed into the following four matrices based on the left and right multipliers:

$$\begin{aligned} \mathbf{Q}_i^{ll} &= \frac{1}{\Delta t} \mathbb{P}^{\Sigma H} \int_{\mathbb{R}} p_i(t) \tilde{\mathfrak{Q}} \left( p_0(t) \mathbf{P}^{\Lambda H} \right) dt \\ &= \mathbb{P}^{\Sigma H} \int_{\mathbb{R}} \delta_i(t) \tilde{\mathfrak{Q}} \left( h_0(t) \mathbf{P}^{\Lambda H} \right) dt, \\ \mathbf{Q}_i^{ls} &= \frac{1}{\Delta t} \mathbb{P}^{\Sigma H} \int_{\mathbb{R}} p_i(t) \tilde{\mathfrak{Q}} \left( h_0(t) \mathbf{P}^\Sigma \right) dt \\ &= \mathbb{P}^{\Sigma H} \int_{\mathbb{R}} \delta_i(t) \tilde{\mathfrak{Q}} \left( q_0(t) \mathbf{P}^\Sigma \right) dt, \\ \mathbf{Q}_i^{sl} &= \mathbb{P}^\Lambda \int_{\mathbb{R}} \delta_i(t) \tilde{\mathfrak{Q}} \left( p_0(t) \mathbf{P}^{\Lambda H} \right) dt, \\ \mathbf{Q}_i^{ss} &= \mathbb{P}^\Lambda \int_{\mathbb{R}} \delta_i(t) \tilde{\mathfrak{Q}} \left( h_0(t) \mathbf{P}^\Sigma \right) dt. \end{aligned}$$

In the first two terms, we used the properties (14) and (18). Please note that each of the four components of  $\mathbf{Q}_i$  is a  $2 \times 2$  block matrix, inheriting the structure of  $\tilde{\mathfrak{Q}}$ .

Now, let us look deeper into each block of each matrix. In particular, we demonstrate how to compute  $\mathbf{Q}_i^{ll}, \mathbf{Q}_i^{ls}, \mathbf{Q}_i^{sl}$  and  $\mathbf{Q}_i^{ss}$  in practice. We note that the diagonal blocks  $\tilde{\mathfrak{Q}}_{11}$  and  $\tilde{\mathfrak{Q}}_{22}$  of  $\tilde{\mathfrak{Q}}$  only involve the TD-EFIOs  $\mathcal{T}$  and  $\mathcal{T}'$ , whereas the off-diagonal blocks  $\tilde{\mathfrak{Q}}_{12}$  and  $\tilde{\mathfrak{Q}}_{21}$  only involve  $\mathcal{K}$  and  $\mathcal{K}'$ . Without loss of generality, we focus on the contributions from  $\mathcal{T}$  and  $\mathcal{K}$  only. The corresponding counterparts of  $\mathcal{T}'$  and  $\mathcal{K}'$  are tagged with a superscript '.

1) *The matrices  $\mathbf{Q}_i^{ll}$  and  $\mathbf{Q}_i^{ss}$ :* The contributions from  $\mathcal{T}$  (to the diagonal blocks) of these matrices are in fact the temporal discretization of  $\mathfrak{Z}_{ll}$  and  $\mathfrak{Z}_{ss}$  in (13), respectively, i.e.,

$$\begin{aligned} \mathbf{Z}_i^{ll} &:= \mathbb{T}^{\Sigma H} \mathbf{G}^{-1} \int_{\mathbb{R}} \delta_i(t) \mathfrak{T}^s \left( h_0(t) \mathbf{P}^{\Lambda H} \right) dt, \\ \mathbf{Z}_i^{ss} &:= \mathbb{T}^\Lambda \mathbf{G}^{-1} \mathbf{P}^{\Lambda H} \int_{\mathbb{R}} \delta_i(t) \mathfrak{T}^s \left( h_0(t) \mathbf{P}^\Sigma \right) dt. \end{aligned}$$

In practice, it is unnecessary (and probably impossible) to firstly discretize  $\mathcal{T}^s$  in space to get  $\mathfrak{T}^s$ , then discretize  $\mathfrak{T}^s$  in time. Instead, one can perform a collocation-in-time Galerkin-in-space discretization of  $\mathcal{T}^s$ . Let  $\mathbf{T}_i$  be the space-time discretization of  $\mathcal{T}^s$ , whose elements are defined by

$$\begin{aligned} [\mathbf{T}_i]_{mn} &:= \int_{\mathbb{R}} \delta_i(t) \langle \mathbf{n} \times \mathbf{f}_m, \mathcal{T}^s (h_0(t) \mathbf{f}_n) \rangle dt \\ &= \langle \mathbf{n} \times \mathbf{f}_m, \mathcal{T}^s (h_0(t) \mathbf{f}_n) \rangle|_{t=i\Delta t}, \end{aligned}$$

with  $m, n = 1, 2, \dots, N_e$ . The matrices  $\mathbf{Z}_i^{ll}$  and  $\mathbf{Z}_i^{ss}$  can be rewritten as follows:

$$\begin{aligned} \mathbf{Z}_i^{ll} &= \mathbb{T}^{\Sigma H} \mathbf{G}^{-1} \mathbf{T}_i \mathbf{P}^{\Lambda H}, \\ \mathbf{Z}_i^{ss} &= \mathbb{T}^\Lambda \mathbf{G}^{-1} \mathbf{P}^{\Lambda H} \mathbf{T}_i \mathbf{P}^\Sigma. \end{aligned}$$

Analogously, we define the matrix  $\mathbf{K}_i$  such that

$$\begin{aligned} [\mathbf{K}_i]_{mn} &:= \int_{\mathbb{R}} \delta_i(t) \langle \mathbf{n} \times \mathbf{f}_m, \mathcal{K} (h_0(t) \mathbf{f}_n) \rangle dt \\ &= \langle \mathbf{n} \times \mathbf{f}_m, \mathcal{K} (h_0(t) \mathbf{f}_n) \rangle|_{t=i\Delta t}, \end{aligned}$$

with  $m, n = 1, 2, \dots, N_e$ . The contributions from  $\mathcal{K}$  to the matrices  $\mathbf{Q}_i^{ll}$  and  $\mathbf{Q}_i^{ss}$  respectively read

$$\begin{aligned} \mathbf{M}_i^{ll} &:= \mathbb{T}^{\Sigma H} \mathbf{G}^{-1} \mathbf{K}_i \mathbf{P}^{\Lambda H}, \\ \mathbf{M}_i^{ss} &:= \mathbb{T}^\Lambda \mathbf{G}^{-1} \mathbf{P}^{\Lambda H} \mathbf{K}_i \mathbf{P}^\Sigma. \end{aligned}$$

Finally, taking into account the contributions from  $\mathcal{T}'$  and  $\mathcal{K}'$ , the matrices  $\mathbf{Q}_i^{ll}$  and  $\mathbf{Q}_i^{ss}$  are constructed as follows:

$$\begin{aligned} \mathbf{Q}_i^{ll} &= \mathbb{T}^{\Sigma H} \mathbf{G}^{-1} \begin{pmatrix} \eta \mathbf{T}_i + \eta' \mathbf{T}_i' & -\mathbf{K}_i - \mathbf{K}_i' \\ \mathbf{K}_i + \mathbf{K}_i' & \frac{1}{\eta} \mathbf{T}_i + \frac{1}{\eta'} \mathbf{T}_i' \end{pmatrix} \mathbf{P}^{\Lambda H}, \\ \mathbf{Q}_i^{ss} &= \mathbb{T}^\Lambda \mathbf{G}^{-1} \mathbf{P}^{\Lambda H} \begin{pmatrix} \eta \mathbf{T}_i + \eta' \mathbf{T}_i' & -\mathbf{K}_i - \mathbf{K}_i' \\ \mathbf{K}_i + \mathbf{K}_i' & \frac{1}{\eta} \mathbf{T}_i + \frac{1}{\eta'} \mathbf{T}_i' \end{pmatrix} \mathbf{P}^\Sigma. \end{aligned}$$

It is noteworthy that  $\mathbf{Q}_i^{ll}$  and  $\mathbf{Q}_i^{ss}$  do not exhibit an infinite tail, since  $\mathcal{T}^s$  and  $\mathcal{K}$  do not contain temporal integration. In particular,  $\mathbf{Q}_i^{ll} = \mathbf{Q}_i^{ss} = \mathbf{0}$  for all  $i > k_{\max} := \lceil \frac{T_{\max}}{\Delta t} \rceil$ .

2) *The matrix  $\mathbf{Q}_i^{ls}$ :* Analogous to  $\mathbf{Q}_i^{ll}$  and  $\mathbf{Q}_i^{ss}$ , we introduce the following matrices:

$$\begin{aligned} [\tilde{\mathbf{T}}_i]_{mn} &:= T_{\max} \int_{\mathbb{R}} \delta_i(t) \langle \mathbf{n} \times \mathbf{f}_m, \partial_t \mathcal{T}(q_0(t) \mathbf{f}_n) \rangle dt \\ &= T_{\max} \langle \mathbf{n} \times \mathbf{f}_m, \partial_t \mathcal{T}(q_0(t) \mathbf{f}_n) \rangle|_{t=i\Delta t}, \\ [\tilde{\mathbf{K}}_i]_{mn} &:= T_{\max} \int_{\mathbb{R}} \delta_i(t) \langle \mathbf{n} \times \mathbf{f}_m, \partial_t \mathcal{K}(q_0(t) \mathbf{f}_n) \rangle dt \\ &= T_{\max} \langle \mathbf{n} \times \mathbf{f}_m, \partial_t \mathcal{K}(q_0(t) \mathbf{f}_n) \rangle|_{t=i\Delta t}, \end{aligned}$$

with  $m, n = 1, 2, \dots, N_e$ . Then, the matrix  $\mathbf{Q}_i^{ls}$  is given by

$$\mathbf{Q}_i^{ls} = \mathbb{T}^{\Sigma H} \mathbf{G}^{-1} \begin{pmatrix} \eta \tilde{\mathbf{T}}_i + \eta' \tilde{\mathbf{T}}_i' & -\tilde{\mathbf{K}}_i - \tilde{\mathbf{K}}_i' \\ \tilde{\mathbf{K}}_i + \tilde{\mathbf{K}}_i' & \frac{1}{\eta} \tilde{\mathbf{T}}_i + \frac{1}{\eta'} \tilde{\mathbf{T}}_i' \end{pmatrix} \mathbf{P}^{\Sigma}.$$

These matrices also do not exhibit an infinite tail because the temporal integration in  $\mathcal{T}^h$  is canceled out by the temporal differentiation in the rescaling factor  $\partial_t$ . However,  $\mathbf{Q}_i^{ls} = \mathbf{0}$  for all  $i > k_{\max} + 1$  rather than  $i > k_{\max}$  for  $\mathbf{Q}_i^{ll}$  and  $\mathbf{Q}_i^{ss}$ , as the support of  $q_0(t)$  exceeds that of  $h_0(t)$  by  $\Delta t$ .

3) *The matrix  $\mathbf{Q}_i^{sl}$ :* Let us denote

$$\begin{aligned} [\tilde{\mathbf{T}}_i]_{mn} &= \frac{1}{T_{\max}} \langle \mathbf{n} \times \mathbf{f}_m, \partial_t^{-1} \mathcal{T}^s(p_0(t) \mathbf{f}_n) \rangle|_{t=i\Delta t}, \\ [\tilde{\mathbf{K}}_i]_{mn} &= \frac{1}{T_{\max}} \langle \mathbf{n} \times \mathbf{f}_m, \partial_t^{-1} \mathcal{K}(p_0(t) \mathbf{f}_n) \rangle|_{t=i\Delta t}, \end{aligned}$$

with  $m, n = 1, 2, \dots, N_e$ . The matrix  $\mathbf{Q}_i^{sl}$  is given by

$$\mathbf{Q}_i^{sl} = \mathbb{T}^{\Lambda} \mathbf{G}^{-1} \mathbf{P}^{\Lambda H} \begin{pmatrix} \eta \tilde{\mathbf{T}}_i + \eta' \tilde{\mathbf{T}}_i' & -\tilde{\mathbf{K}}_i - \tilde{\mathbf{K}}_i' \\ \tilde{\mathbf{K}}_i + \tilde{\mathbf{K}}_i' & \frac{1}{\eta} \tilde{\mathbf{T}}_i + \frac{1}{\eta'} \tilde{\mathbf{T}}_i' \end{pmatrix} \mathbf{P}^{\Lambda H}.$$

Whereas the matrices  $\tilde{\mathbf{T}}_i$  and  $\tilde{\mathbf{T}}_i'$  do not exhibit an infinite tail (i.e.,  $\tilde{\mathbf{T}}_i = \tilde{\mathbf{T}}_i' = \mathbf{0}$  for all  $i > k_{\max} - 1$ ),  $\tilde{\mathbf{K}}_i$  and  $\tilde{\mathbf{K}}_i'$  do because  $\partial_t^{-1} \mathcal{K}$  and  $\partial_t^{-1} \mathcal{K}'$  contain the temporal integration. It is now shown that by virtue of the serendipitous interplay between the temporal rescaling operators on one hand, and the Helmholtz splitting on the other, this tail eventually does not lead to an infinite number of non-zero matrices  $\mathbf{Q}_i^{sl}$ . Indeed, we note that

$$\partial_t^{-1} p_0(t) = \begin{cases} 0 & t \leq -\Delta t, \\ t + \Delta t & -\Delta t < t \leq 0, \\ \Delta t & \text{otherwise.} \end{cases}$$

It implies the constant tail  $\tilde{\mathbf{K}}_i = \tilde{\mathbf{K}}_i' = \frac{\Delta t}{T_{\max}} \mathbb{K}_0$  for all  $i > k_{\max} - 1$ , where

$$[\mathbb{K}_0]_{mn} = \langle \mathbf{n} \times \mathbf{f}_m, K_0 \mathbf{f}_n \rangle,$$

with  $m, n = 1, 2, \dots, N_e$ , and the static MFIE operator

$$(K_0 \mathbf{j})(\mathbf{x}) = \mathbf{n} \times p.v. \int_{\Gamma} \mathbf{curl}_{\mathbf{x}} \frac{\mathbf{j}(\mathbf{y})}{4\pi |\mathbf{x} - \mathbf{y}|} ds_{\mathbf{y}}.$$

In fact,  $K_0$  is the limit of the frequency-domain MFIE operator  $K_{\kappa}$  when the wavenumber  $\kappa \rightarrow 0$ . Hence, one can deduce from the large-timestep scaling of the off-diagonal blocks of  $\tilde{\mathbf{Q}}$  (by setting  $\omega = 0$ ) that

$$\mathbb{T}^{\Lambda} \mathbf{G}^{-1} \mathbf{P}^{\Lambda H} \mathbb{K}_0 \mathbf{P}^{\Lambda H} = \mathbf{0}.$$

This property can also be deduced from [33]. Combining all properties together, we have

$$\mathbb{T}^{\Lambda} \mathbf{G}^{-1} \mathbf{P}^{\Lambda H} \tilde{\mathbf{K}}_i \mathbf{P}^{\Lambda H} = \mathbb{T}^{\Lambda} \mathbf{G}^{-1} \mathbf{P}^{\Lambda H} \tilde{\mathbf{K}}_i' \mathbf{P}^{\Lambda H} = \mathbf{0}, \quad (19)$$

for all  $i > k_{\max} - 1$ . Therefore,  $\mathbf{Q}_i^{sl} = \mathbf{0}$  for all  $i > k_{\max} - 1$ . In practice, the integrals are typically approximated using quadrature rules, which introduces numerical errors into the interaction matrices. As a result, the matrices in (19) may not vanish. To address this, they should be explicitly set to zero, thereby reducing both computational time and memory usage. Numerical experiments further show that this strategy also improves the accuracy and stability of the solution.

### C. Computation of Right-Hand Side

The right-hand side vectors in (15) are defined by

$$\mathbf{r}_i = \int_{\mathbb{R}} \left( \frac{p_i(t)}{\Delta t} \mathbb{P}^{\Sigma H} + \delta_i(t) \mathbb{P}^{\Lambda} \right) \mathbb{L} \mathbf{T} \mathbf{G}^{-1} \begin{pmatrix} \mathbf{e}(t) \\ \mathbf{h}(t) \end{pmatrix} dt, \quad (20)$$

with  $i = 1, 2, \dots, N_t$ , which consist of the loop contribution

$$\mathbf{r}_i^l := \frac{1}{\Delta t} \mathbb{T}^{\Sigma H} \mathbf{G}^{-1} \int_{\mathbb{R}} p_i(t) \begin{pmatrix} \mathbf{e}(t) \\ \mathbf{h}(t) \end{pmatrix} dt,$$

and the star contribution

$$\begin{aligned} \mathbf{r}_i^s &:= \frac{1}{T_{\max}} \mathbb{T}^{\Lambda} \mathbf{G}^{-1} \mathbf{P}^{\Lambda H} \int_{\mathbb{R}} \delta_i(t) \left( \frac{\partial_t^{-1} \mathbf{e}(t)}{\partial_t^{-1} \mathbf{h}(t)} \right) dt \\ &= \frac{1}{T_{\max}} \mathbb{T}^{\Lambda} \mathbf{G}^{-1} \mathbf{P}^{\Lambda H} \left( \frac{\partial_t^{-1} \mathbf{e}(t)}{\partial_t^{-1} \mathbf{h}(t)} \right) \Big|_{t=i\Delta t}. \end{aligned}$$

Let us assume the incident transient fields  $\mathbf{e}^{in}$  and  $\mathbf{h}^{in}$  are Gaussian-in-time plane wave, i.e.,

$$\begin{aligned} \mathbf{e}^{in}(\mathbf{x}, t) &= \frac{4A}{w\sqrt{\pi}} \mathbf{p} \exp \left( - \left( \frac{4}{w} (c(t - t_0) - \mathbf{k} \cdot \mathbf{x}) \right)^2 \right), \\ \mathbf{h}^{in}(\mathbf{x}, t) &= \eta^{-1} \mathbf{k} \times \mathbf{e}^{in}(\mathbf{x}, t), \end{aligned} \quad (21)$$

where  $A$  is the amplitude,  $\mathbf{p}$  is the polarization,  $\mathbf{k}$  is the direction,  $w$  is the width, and  $t_0$  is the time of arrival. It is clear that the loop component  $\mathbf{r}_i^l$  exponentially decays as the incident fields at late times, whereas the star component  $\mathbf{r}_i^s$  exponentially approaches a constant since

$$\frac{4A}{w\sqrt{\pi}} \mathbf{p} \int_{\mathbb{R}} \exp \left( - \left( \frac{4}{w} (c(t - t_0) - \mathbf{k} \cdot \mathbf{x}) \right)^2 \right) dt = \frac{A}{c} \mathbf{p}.$$

In fact, the approaching constant is also zero, as the gradient of a constant field is zero. In practice, however,  $\mathbf{r}_i^s$  may not decay due to numerical errors and should be explicitly set to zero to yield stable and accurate solutions [44]. In the time-domain implementation, it can easily be done by truncating the star component  $\mathbf{r}_i^s$  at late times, a procedure reminiscent of the truncation of the off-diagonal blocks of  $\mathbf{Q}_i^{sl}$ .

In conclusion, (15) is the preconditioned and regularized TD-PMCHWT formulation (shorten as qHP TD-PMCHWT), with the right-hand side vectors defined by (20) and the matrix blocks computed as follows:

$$\mathbf{Q}_i = \mathbf{Q}_i^{ll} + \mathbf{Q}_i^{ls} + \mathbf{Q}_i^{sl} + \mathbf{Q}_i^{ss},$$

where  $\mathbf{Q}_i = \mathbf{0}$  for all  $i > k_{\max} + 1$ .

## VI. NUMERICAL RESULTS

In this section, we perform some experiments to corroborate the effectiveness of the proposed qHP TD-PMCHWT formulation (15). The numerical experiments involve homogeneous dielectric objects of three geometries, which exhibit different topological and smoothness challenges (see Fig. 1):

- (a) A sphere of radius 1m (smooth and simply-connected);
- (b) A torus of two radii 0.75m and 0.25m (smooth and multiply-connected);
- (c) A star-based pyramid of height 0.5m and 24-pointed star base, whose vertices lie on two concentric circles of radius 1m and 0.3m (highly non-smooth) [45].

In all cases, the background medium is free space, and the excitation is a Gaussian-in-time plane wave defined in (21), with parameters  $A = 1\text{V}$ ,  $\mathbf{p} = \mathbf{1}_x$ ,  $\mathbf{k} = \mathbf{1}_z$ ,  $w = 120c\Delta t$ , and  $t_0 = 240\Delta t$ , where the timestep  $\Delta t$  will be specified later for each experiment. A semi-analytic quadrature strategy is employed to discretize time-domain integral operators. The inner integral is evaluated using the Wilton technique [46] and its generalization to the calculation of interactions through retarded potentials by Shanker et al. [23], while the outer (test) integral is computed numerically using  $N_q$  quadrature points.

### A. Late-Time Stability

We start with examining the late-time stability of the proposed qHP TD-PMCHWT formulation through extended versions of the test cases performed in [31].

As the first example, we consider the scattering by a unit dielectric sphere. The unit sphere is approximated by a triangular mesh consisting of 476 triangles, 240 vertices, and 714 edges. The interior domain is also free space, i.e.,  $(\epsilon', \mu') = (\epsilon, \mu)$ . In this case, the tangential traces of the incident fields  $(\mathbf{j}, \mathbf{m}) = (\mathbf{n} \times \mathbf{h}^{in}, \mathbf{e}^{in} \times \mathbf{n})$  are the exact solution to the scattering problem. To facilitate comparison with numerical solutions, the exact solution is projected into the RWG space as follows:

$$\begin{pmatrix} \mathbf{j}_i^{ext} \\ \mathbf{m}_i^{ext} \end{pmatrix} = -\mathbf{G}^{-\top} \begin{pmatrix} \mathbf{h}_i \\ \mathbf{e}_i \end{pmatrix},$$

with

$$\begin{pmatrix} [\mathbf{h}_i]_m \\ [\mathbf{e}_i]_m \end{pmatrix} = \int_{\Gamma} \mathbf{g}_m(\mathbf{x}) \cdot \begin{pmatrix} \mathbf{h}^{in}(\mathbf{x}, i\Delta t) \\ -\mathbf{e}^{in}(\mathbf{x}, i\Delta t) \end{pmatrix} ds,$$

for all  $i = 1, 2, \dots, N_t$ , and  $m = 1, 2, \dots, N_e$ . The timestep used in this simulation is  $\Delta t = 3.336\text{ns}$  (or  $c\Delta t = 1\text{m}$ ).

Fig. 2 (*left*) compares the projected exact solution with numerical solutions to the classical TD-PMCHWT equation (1) and the qHP TD-PMCHWT (15). The TD-PMCHWT equation is discretized via a collocation-in-time Galerkin-in-space scheme, as described in [31], with different quadrature strategies employed. As shown in Fig. 2 (*left*), the classical TD-PMCHWT suffers from late-time instability, which manifests as non-decaying or even exponentially growing errors. This instability is highly sensitive to numerical errors in the computation of interaction matrices [31]. The proposed qHP TD-PMCHWT formulation, in contrast, produces a stable solution that closely matches the exact one, with discrepancies on

the order of machine precision ( $\approx 10^{-15}$  in double precision). Notably, this stable and accurate solution is obtained when using a low-precision quadrature in the integral evaluations.

Next, we investigate the scattering by a dielectric torus. The interior domain is filled by a medium with  $(\epsilon', \mu') = (3\epsilon, \mu)$ . The surface  $\Gamma$  is discretized by 952 triangles with 476 vertices and 1428 edges, while the time interval is equidistantly discretized by timestep  $c\Delta t = 2\text{m}$ . Fig. 2 (*middle*) presents numerical electric current densities  $\mathbf{j}$  computed from the TD-PMCHWT equation and the qHP TD-PMCHWT. Whereas the numerical solutions to the TD-PMCHWT are unstable at late times, the solution to the qHP TD-PMCHWT is stable. This result confirms the robustness of the proposed formulation when applied to multiply-connected geometries.

The last example involves a highly non-smooth domain, named star-based pyramid [45]. This geometry features very sharp corners and edges, which significantly amplify numerical quadrature errors in the time-domain discretization [31]. The surface is triangulated into 1542 triangles with 773 vertices and 2313 edges. The pyramid is filled by medium with  $(\epsilon', \mu') = (5\epsilon, \mu)$ , and the timestep  $c\Delta t = 5\text{m}$ . As illustrated in Fig. 2 (*right*), numerical solutions to the TD-PMCHWT on this surface are severely unstable, exhibiting very high growth rates even when the integrals are computed using extremely accurate quadrature rules. In contrast, the qHP TD-PMCHWT yields a stable solution with very few quadrature points, corroborating the high efficiency of the proposed method.

The stability behavior of the classical TD-PMCHWT and the proposed qHP TD-PMCHWT is further analyzed by performing the companion matrix stability analysis. This technique was first proposed in [47], and recently extended for time-domain integral systems with constant infinite tails (e.g., TD-EFIE and TD-PMCHWT) in [31], [48]. Fig. 3 shows the spectra of the companion matrices for the TD-PMCHWT and qHP TD-PMCHWT systems in the previous three examples. The companion matrices of the TD-PMCHWT exhibit eigenvalues clustered around  $1 + 0\iota$ , with some shifted outside the unit circle due to numerical errors causing instability in the numerical solution. In contrast, all eigenvalues of the qHP TD-PMCHWT reside strictly inside the unit circle with none located near  $1 + 0\iota$ , demonstrating that the qHP TD-PMCHWT is immune to late-time instability.

### B. Conditioning

We continue with examining the conditioning properties of the proposed formulation. First, the average mesh size is fixed at  $h = 0.3\text{m}$  for the sphere,  $h = 0.15\text{m}$  for the torus, and  $h = 0.16\text{m}$  for the star-based pyramid. The condition number of  $\mathbf{Q}_0$  – the matrix that appears on the left-hand side of the MOT system (16) that needs to be solved at each time step – is computed with timesteps  $c\Delta t$  ranging from  $1\text{m}$  to  $512\text{m}$ . As illustrated in Fig. 4 (*left*), the condition number of the classical TD-PMCHWT system grows quadratically with  $\Delta t$ , whereas that of the qHP TD-PMCHWT remains constant.

Next, we fix the timestep  $c\Delta t = 1\text{m}$  for the sphere and  $c\Delta t = 2\text{m}$  for the torus, and decrease the mesh size  $h$  from  $0.31\text{m}$  to  $0.06\text{m}$ . The condition number of matrix systems as

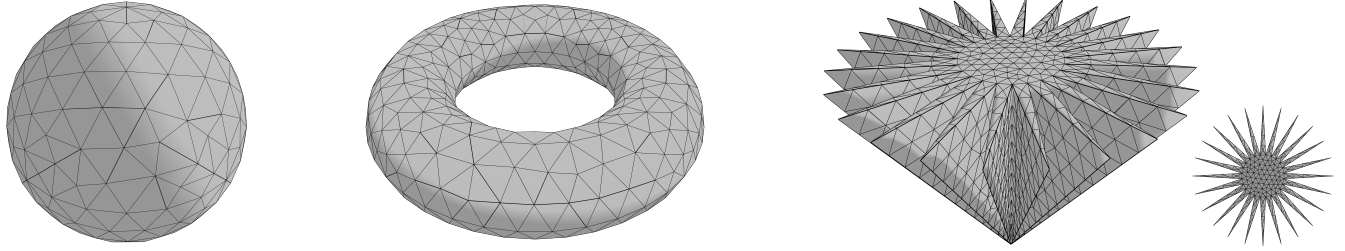


Fig. 1. Scatterer geometries used in numerical experiments. From left to right: a smooth and simply-connected sphere of radius 1m; a smooth and multiply-connected torus of 2 radii 0.75m and 0.25m; and a highly non-smooth star-based pyramid of height 0.5m, with 24 vertices of the base lie on two concentric circles of radius 1m and 0.3m.

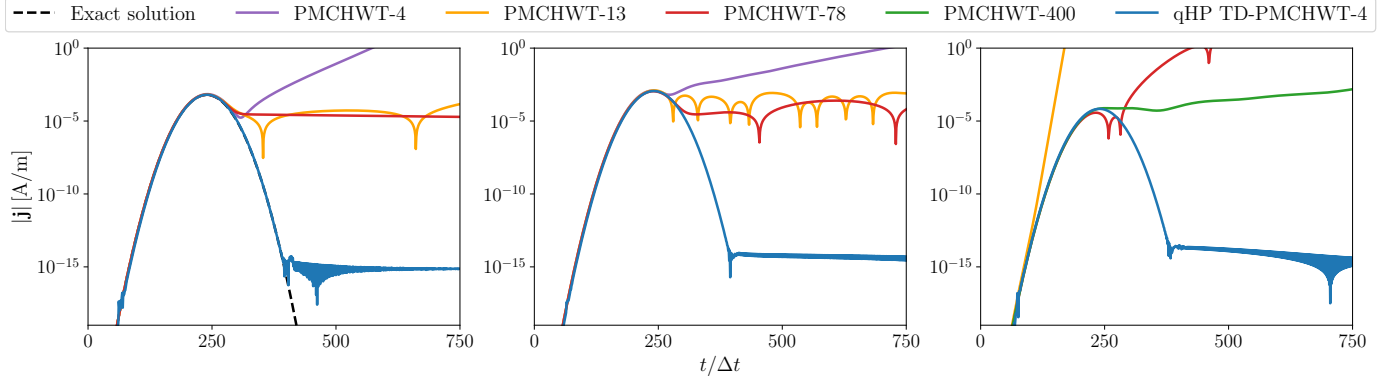


Fig. 2. Intensity of the electric current density  $j$  on the unit sphere, the toroidal surface, and the star-based pyramid (from left to right). Different quadrature strategies are employed to discretize the classical TD-PMCHWT formulation, characterized by the number of quadrature points  $N_q = 4, 13, 78$ , and 400 appearing on the legends. Numerical solutions to the TD-PMCHWT equation are severely unstable at late times and highly sensitive to quadrature errors. In contrast, the solution to the proposed qHP TD-PMCHWT formulation is stable even when the integrals are computed with a very low precision. In all three cases, only  $N_q = 4$  quadrature points are used when discretizing the qHP TD-PMCHWT.

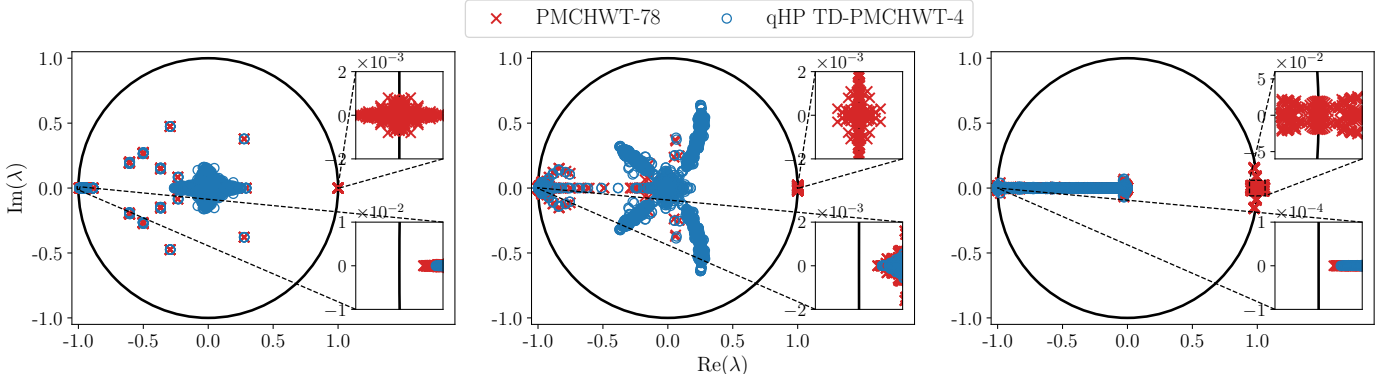


Fig. 3. Spectra of the companion matrices for the TD-PMCHWT (discretized using  $N_q = 78$  quadrature points) and the proposed qHP TD-PMCHWT ( $N_q = 4$ ), on the unit sphere, the toroidal surface, and the star-based pyramid (from left to right). The TD-PMCHWT's spectra exhibit eigenvalues clustered around  $1 + 0i$  that cause late-time instability to numerical solution. In contrast, the qHP TD-PMCHWT does not support any eigenvalue around  $1 + 0i$ , rendering its solution stable. In all cases, the eigenvalues near  $-1 + 0i$  are unproblematic as they reside strictly inside the unit circle, and correspond to the oscillation of the solution below the machine precision [29].

functions of  $h$  are presented in Fig. 4 (middle), confirming the well-conditioning of the qHP TD-PMCHWT when the spatial mesh density is increased.

Due to the complex geometry of the star-based pyramid, we are unable to reach the dense-mesh asymptotic regime with the available hardware. Instead, we solve the scattering problem on this structure using the MOT scheme combined with a GMRES iterative solver, and report the corresponding GMRES convergence histories in Fig. 4 (right). The TD-PMCHWT

system fails to reach  $10^{-6}$  accuracy in 800 iterations, whereas the qHP TD-PMCHWT converges within  $10^{-8}$  tolerance in only 56 iterations. These results corroborate that the proposed qHP TD-PMCHWT formulation yields well-conditioned matrix systems that can be efficiently solved using the MOT scheme and iterative solvers.

#### C. Far-Field Computation

In the final experiment, we assess the accuracy of scattered far fields obtained from the qHP TD-PMCHWT solution at

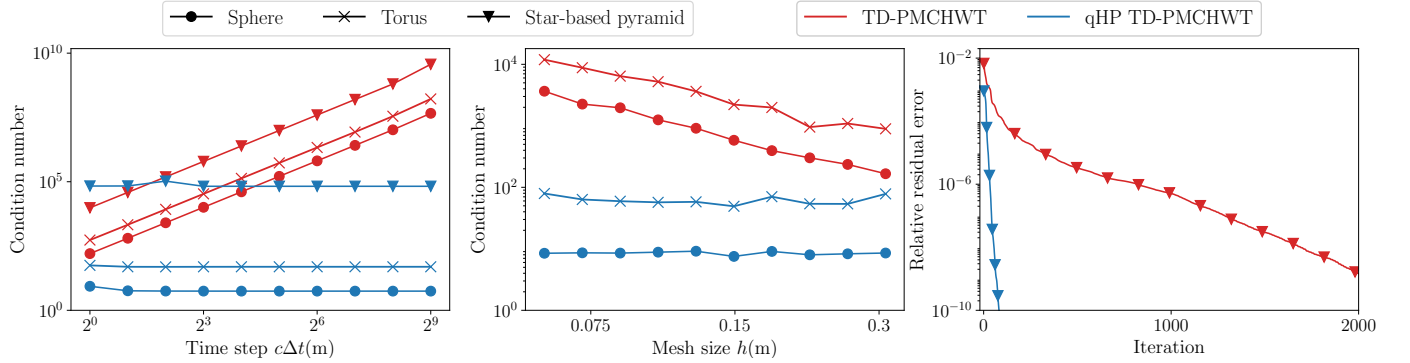


Fig. 4. (Left) Condition number of the TD-PMCHWT and qHP TD-PMCHWT systems for scattering by the unit sphere, the torus, and the star-based pyramid as a function of the timestep  $\Delta t$ . (Middle) Condition number of the TD-PMCHWT and qHP TD-PMCHWT systems for scattering by the sphere and the torus as a function of the mesh size  $h$ . (Right) Convergence history for the GMRES solution of the star-based pyramid scattering problem. The classical TD-PMCHWT formulation suffers from dense-mesh breakdown and large-timestep breakdown, whereas the proposed qHP TD-PMCHWT formulation is immune to both of them.

low frequencies. The surface current densities  $\mathbf{j}$  and  $\mathbf{m}$  are computed on a triangular mesh (with  $h = 0.2\text{m}$ ) of the unit sphere with timestep  $\Delta t = 100\text{s}$  (or  $c\Delta t = 2.998 \times 10^{10}\text{m}$ ), and subsequently Fourier transformed at  $10^{-5}\text{Hz}$ .

Fig. 5 shows the scattered electric far field derived from the numerical surface currents of the qHP TD-PMCHWT, which closely matches the reference Mie-series solution [49]. In contrast, the far field computed from the FD-PMCHWT solution is completely wrong, due to the significant loss of accuracy in the surface currents at low frequencies. This result confirms the accuracy of the proposed formulation.

A direct comparison with the TD-PMCHWT formulation is not meaningful here, as its time-domain solutions fail to decay at late times, producing highly inaccurate frequency-domain surface currents after Fourier transformation. A frequency-domain counterpart of the proposed formulation was presented in [14], demonstrating similar performance in mitigating breakdowns and improving solution accuracy.

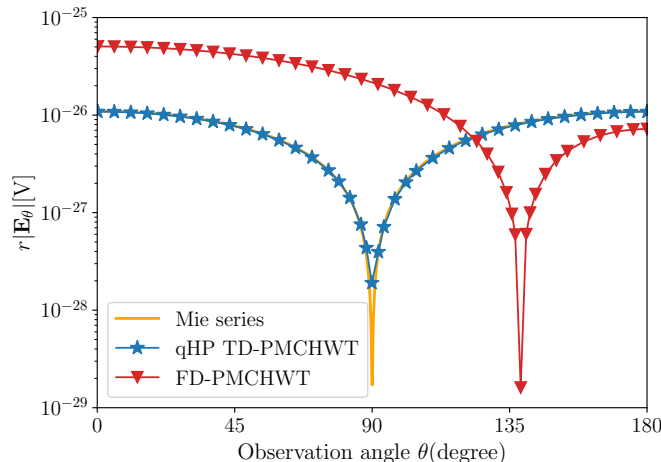


Fig. 5. Scattered electric far field of the incident plane wave with the frequency  $10^{-5}\text{Hz}$ , computed using the Mie series, the qHP TD-PMCHWT and the FD-PMCHWT. The far field computed from the qHP TD-PMCHWT is accurate, whereas the one computed from the FD-PMCHWT is completely wrong due to the loss of solution accuracy at low frequencies.

## VII. CONCLUSION

We have proposed a new time-domain formulation for electromagnetic scattering by dielectric objects, building upon the TD-PMCHWT equation and the loop-star decomposition via quasi-Helmholtz projectors. A multiplicative diagonal preconditioner, based on a modified static EFIO, was introduced to eliminate the dense-mesh breakdown of the TD-PMCHWT equation. The large-timestep breakdown and the loss of solution accuracy were simultaneously mitigated through a rescaling procedure, while incorporating temporal integration and differentiation as rescaling factors effectively suppressed the notorious late-time instability. An appropriate temporal testing scheme was applied, with particular attention to practical implementation. Numerical experiments across various scenarios confirmed the accuracy, stability, and robustness of the proposed formulation. The robustness against numerical quadrature errors becomes even more critical when employing compression techniques, such as plane-wave time-domain algorithms, as they unavoidably introduce errors that are similar to quadrature errors.

Future research may explore advanced discretization schemes to further enhance performance, such as higher-order spatial and temporal basis functions or time discretizations based on convolution quadrature.

## REFERENCES

- [1] A. J. Poggio and E. K. Miller, *Integral equation solutions of three-dimensional scattering problems*. Elsevier Science & Technology, 1973, pp. 159–264.
- [2] C. Müller, *Foundations of the mathematical theory of electromagnetic waves*. Springer Berlin Heidelberg, 1969.
- [3] P. Ylä-Oijala, M. Taskinen, and S. Järvenpää, “Analysis of surface integral equations in electromagnetic scattering and radiation problems,” *Eng. Anal. Bound. Elem.*, vol. 32, no. 3, pp. 196–209, 2008.
- [4] S. Yan, J.-M. Jin, and Z. Nie, “Accuracy improvement of the second-kind integral equations for generally shaped objects,” *IEEE Trans. Antennas Propag.*, vol. 61, no. 2, pp. 788–797, 2013.
- [5] R. Hiptmair, “Operator preconditioning,” *Comput. Math. Appl.*, vol. 52, no. 5, pp. 699–706, 2006.
- [6] S. Yan, J.-M. Jin, and Z. Nie, “A comparative study of Calderón preconditioners for PMCHWT equations,” *IEEE Trans. Antennas Propag.*, vol. 58, no. 7, pp. 2375–2383, 2010.

[7] K. Cools, F. P. Andriulli, and E. Michielssen, "A Calderón multiplicative preconditioner for the PMCHWT integral equation," *IEEE Trans. Antennas Propag.*, vol. 59, no. 12, pp. 4579–4587, 2011.

[8] K. Niino and N. Nishimura, "Calderón preconditioning approaches for PMCHWT formulations for Maxwell's equations," *Int. J. Numer. Model.: Electron. Netw. Devices Fields*, vol. 25, pp. 558–572, 2012.

[9] A. Kleanthous, T. Betcke, D. P. Hewett, P. Escapil-Inchauspé, C. Jerez-Hanckes, and A. J. Baran, "Accelerated Calderón preconditioning for Maxwell transmission problems," *J. Comput. Phys.*, vol. 458, p. 111099, 2022.

[10] V. C. Le, P. Cordel, F. P. Andriulli, and K. Cools, "A Yukawa-Calderón time-domain combined field integral equation for electromagnetic scattering," in *Proc. Int. Conf. Electromagn. Adv. Appl. (ICEAA)*, 2023.

[11] —, "A stabilized time-domain combined field integral equation using the quasi-Helmholtz projectors," *IEEE Trans. Antennas Propag.*, vol. 72, no. 7, pp. 5852–5864, 2024.

[12] K. Cools, F. P. Andriulli, F. Olyslager, and E. Michielssen, "Time domain Calderón identities and their application to the integral equation analysis of scattering by PEC objects Part I: Preconditioning," *IEEE Trans. Antennas Propag.*, vol. 57, no. 8, pp. 2352–2364, 2009.

[13] F. P. Andriulli, K. Cools, I. Bogaert, and E. Michielssen, "On a well-conditioned electric field integral operator for multiply connected geometries," *IEEE Trans. Antennas Propag.*, vol. 61, no. 4, pp. 2077–2087, 2013.

[14] Y. Beghein, R. Mitharwal, K. Cools, and F. P. Andriulli, "On a low-frequency and refinement stable PMCHWT integral equation leveraging the quasi-Helmholtz projectors," *IEEE Trans. Antennas Propag.*, vol. 65, no. 10, pp. 5365–5375, 2017.

[15] J. E. O. Guzman, S. B. Adrian, R. Mitharwal, Y. Beghein, T. F. Eibert, K. Cools, and F. P. Andriulli, "On the hierarchical preconditioning of the PMCHWT integral equation on simply and multiply connected geometries," *IEEE Trans. Antennas Propag.*, vol. 16, pp. 1044–1047, 2017.

[16] A. Merlini, Y. Beghein, K. Cools, E. Michielssen, and F. P. Andriulli, "Magnetic and combined field integral equations based on the quasi-Helmholtz projectors," *IEEE Trans. Antennas Propag.*, vol. 68, no. 5, pp. 3834–3846, 2020.

[17] V. Giunzioni, A. Scazzola, A. Merlini, and F. P. Andriulli, "Low-frequency stabilizations of the PMCHWT equation for dielectric and conductive media: On a full-wave alternative to eddy-current solvers," *IEEE Trans. Antennas Propag.*, vol. 73, no. 8, pp. 5725–5740, 2025.

[18] Y. Beghein, K. Cools, and F. P. Andriulli, "A DC stable and large-time step well-balanced TD-EFIE based on quasi-Helmholtz projectors," *IEEE Trans. Antennas Propag.*, vol. 63, no. 7, pp. 3087–3097, 2015.

[19] —, "A DC-stable, well-balanced, Calderón preconditioned time domain electric field integral equation," *IEEE Trans. Antennas Propag.*, vol. 63, no. 12, pp. 5650–5660, 2015.

[20] —, "A robust and low frequency stable time domain PMCHWT equation," in *Proc. Int. Conf. Electromagn. Adv. Appl. (ICEAA)*, 2015, pp. 954–957.

[21] A. Dely, F. P. Andriulli, and K. Cools, "Large time step and DC stable TD-EFIE discretized with implicit Runge-Kutta methods," *IEEE Trans. Antennas Propag.*, vol. 68, no. 2, pp. 976–985, 2020.

[22] H. Mieras and C. Bennett, "Space-time integral equation approach to dielectric targets," *IEEE Trans. Antennas Propag.*, vol. 30, no. 1, pp. 2–9, 1982.

[23] B. Shanker, M. Lu, J. Yuan, and E. Michielssen, "Time domain integral equation analysis of scattering from composite bodies via exact evaluation of radiation fields," *IEEE Trans. Antennas Propag.*, vol. 57, no. 5, pp. 1506–1520, 2009.

[24] Y. Beghein, "Advanced discretization and preconditioning techniques for electromagnetic boundary integral equations," Ph.D. dissertation, Ghent University, 2015.

[25] V. C. Le, F. P. Andriulli, and K. Cools, "A DC stable, well-conditioned and low-frequency regularized time-domain PMCHWT equation," in *Proc. 2024 IEEE Int. Symp. Antennas Propag. and USNC-URSI Radio Sci. Meet.*, 2024.

[26] A. Sadigh and E. Arvas, "Treating the instabilities in marching-on-in-time method from a different perspective (electromagnetic scattering)," *IEEE Trans. Antennas Propag.*, vol. 41, no. 12, pp. 1695–1702, 1993.

[27] D. S. Weile, G. Pisharody, N.-W. Chen, B. Shanker, and E. Michielssen, "A novel scheme for the solution of the time-domain integral equations of electromagnetics," *IEEE Trans. Antennas Propag.*, vol. 52, no. 1, pp. 283–295, 2004.

[28] A. C. Yucel and A. A. Ergin, "Exact evaluation of retarded-time potential integrals for the RWG bases," *IEEE Trans. Antennas Propag.*, vol. 54, no. 5, pp. 1496–1502, 2006.

[29] E. van 't Wout, D. R. van der Heul, H. van der Ven, and C. Vuik, "The influence of the exact evaluation of radiation fields in finite precision arithmetic on the stability of the time domain integral equation method," *IEEE Trans. Antennas Propag.*, vol. 61, no. 12, pp. 6064–6074, 2013.

[30] X. Tian, G. Xiao, and S. Xiang, "Application of analytical expressions for retarded-time potentials in analyzing the transient scattering by dielectric objects," *IEEE Antennas Wirel. Propag. Lett.*, vol. 13, pp. 1313–1316, 2014.

[31] V. C. Le, V. Giunzioni, P. Cordel, F. P. Andriulli, and K. Cools, "On the late-time instability of MOT solution to the time-domain PMCHWT equation," *IEEE Antennas Wirel. Propag. Lett. (Early Access)*, pp. 1–5, 2025.

[32] J.-S. Zhao and W. C. Chew, "Integral equation solution of Maxwell's equations from zero frequency to microwave frequencies," *IEEE Trans. Antennas Propag.*, vol. 48, no. 10, pp. 1635–1645, 2000.

[33] S. Y. Chen, W. C. Chew, J. M. Song, and J.-S. Zhao, "Analysis of low frequency scattering from penetrable scatterers," *IEEE Trans. Geosci. Remote Sens.*, vol. 39, no. 4, pp. 726–735, 2001.

[34] I. Bogaert, K. Cools, F. P. Andriulli, and H. Bagci, "Low-frequency scaling of the standard and mixed magnetic field and Müller integral equations," *IEEE Trans. Antennas Propag.*, vol. 62, no. 2, pp. 822–831, 2014.

[35] F. P. Andriulli, "Loop-star and loop-tree decompositions: Analysis and efficient algorithms," *IEEE Trans. Antennas Propag.*, vol. 60, no. 5, pp. 2347–2356, 2012.

[36] S. Rao, D. Wilton, and A. Glisson, "Electromagnetic scattering by surfaces of arbitrary shape," *IEEE Trans. Antennas Propag.*, vol. AP-30, no. 3, pp. 409–418, 1982.

[37] R. Hiptmair and C. Schwab, "Natural boundary element methods for the electric field integral equation on polyhedra," *SIAM J. Numer. Anal.*, vol. 40, no. 1, pp. 66–86, 2003.

[38] A. Buffa and S. H. Christiansen, "A dual finite element complex on the barycentric refinement," *Math. Comp.*, vol. 76, no. 260, pp. 1743–1770, 2007.

[39] A. Buffa, "Hodge decompositions on the boundary of nonsmooth domains: the multi-connected case," *Math. Models Methods Appl. Sci.*, vol. 11, no. 09, pp. 1491–1503, 2001.

[40] A. Buffa and P. Ciarlet, "On traces for functional spaces related to Maxwell's equations Part II: Hodge decompositions on the boundary of Lipschitz polyhedra and applications," *Math. Methods Appl. Sci.*, vol. 24, pp. 31–48, 2001.

[41] A. Buffa, R. Hiptmair, T. von Petersdorff, and C. Schwab, "Boundary element methods for Maxwell transmission problems in Lipschitz domains," *Numer. Math.*, vol. 95, no. 3, pp. 459–485, 2003.

[42] V. C. Le and K. Cools, "An operator preconditioned combined field integral equation for electromagnetic scattering," *SIAM J. Numer. Anal.*, vol. 62, no. 6, pp. 2484–2505, 2024.

[43] B. Hofmann, T. F. Eibert, F. P. Andriulli, and S. B. Adrian, "An excitation-aware and self-adaptive frequency normalization for low-frequency stabilized electric field integral equation formulations," *IEEE Trans. Antennas Propag.*, vol. 71, no. 5, pp. 4301–4314, 2023.

[44] S. B. Adrian, A. Dely, D. Consoli, A. Merlini, and F. P. Andriulli, "Electromagnetic integral equations: insights in conditioning and preconditioning," *IEEE Open J. Antennas Propag.*, vol. 2, pp. 1143–1174, 2021.

[45] V. C. Le and K. Cools, "Boundary element methods for the magnetic field integral equation on polyhedra," *preprint*, 2024.

[46] D. Wilton, S. Rao, A. Glisson, D. Schaubert, O. Al-Bundak, and C. Butler, "Potential integrals for uniform and linear source distributions on polygonal and polyhedral domains," *IEEE Trans. Antennas Propag.*, vol. 32, no. 3, pp. 276–281, 1984.

[47] S. J. Dodson, S. P. Walker, and M. J. Bluck, "Implicitness and stability of time domain integral equation scattering analyses," *Appl. Comput. Electromagn. Soc. J.*, vol. 13, no. 3, pp. 291–301, 1998.

[48] P. Van Diepen, R. J. Dilz, P. Zwamborn, and M. C. Van Beurden, "The role of Jordan blocks in the MOT-scheme time domain EFIE linear-in-time solution instability," *Prog. Electromagn. Res.*, vol. 95, pp. 123–140, 2022.

[49] B. Hofmann, P. Respondek, and S. B. Adrian, "SphericalScattering: A Julia package for electromagnetic scattering from spherical objects," *J. Open Source Softw.*, vol. 8, no. 91, p. 5820, 2023.